

Crust and Upper Mantle Structure Beneath the Eastern United States

Chengping Chai¹, Charles J. Ammon², Monica Maceira¹, Robert Herrmann³

¹Oak Ridge National Laboratory, Oak Ridge, Tennessee, U.S.A.

²Department of Geosciences, Pennsylvania State University, University Park, Pennsylvania, U.S.A.

³Department of Earth and Atmospheric Sciences, Saint Louis University, St. Louis, Missouri, U.S.A.

Corresponding author: Chengping Chai (chaic@ornl.gov)

Key Points:

- Inverting smoothed receiver functions, surface-wave dispersion and gravity for a 3D shear wave velocity model for the eastern US
- Our velocity model is broadly consistent with published results for the region
- Earthquakes often but not universally locate near areas with seismic speed variation, but not all velocity changes are loci of seismicity

20 **Abstract**

21 The Eastern United States has a complex geological history and hosts several seismic active
22 regions. We investigate the subsurface structure beneath the broader eastern United States. To
23 produce reliable images of the subsurface, we simultaneously invert smoothed P-wave receiver
24 functions, Rayleigh-wave phase and group velocity measurements, and Bouguer gravity
25 observations for the 3D shear wave speed. Using surface-wave observations (3-250 s) and
26 spatially smoothed receiver functions, our velocity models are robust, reliable, and rich in detail.
27 The shear-wave velocity models fit all three types of observations well. The resulting velocity
28 model for the eastern U.S. shows thinner crust beneath New England, the east coast, and the
29 Mississippi Embayment. A relatively thicker crust was found beneath the stable North America
30 craton. A relatively slower upper mantle was imaged beneath New England, the east coast, and
31 western Mississippi Embayment. A comparison of crust thickness derived from our model
32 against four recent published models shows first-order consistency. A relatively small upper
33 mantle low-speed region correlates with a published P-waves analysis that has associated the
34 anomaly with a 75 Ma kimberlite volcanic site in Kentucky. We also explored the relationship
35 between the subsurface structure and seismicity in the eastern U.S. We found earthquakes often
36 locate near regions with seismic velocity variations, but not universally. Not all regions of
37 significant subsurface wave speed changes are loci of seismicity. A weak correlation between
38 upper mantle shear velocity and earthquake focal mechanism has been observed.

39 **Plain Language Summary**

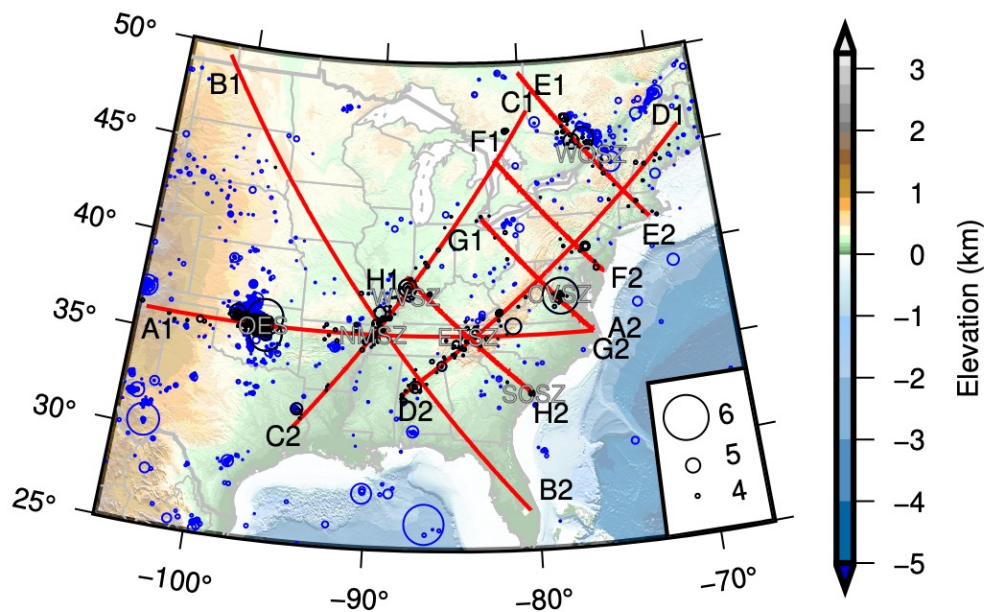
40 The Eastern United States experienced a complex series of geological activities. Earthquakes in
41 the Eastern United States have been recorded at several localized regions. A detailed subsurface
42 structure can help us recover the geological history and studying earthquakes. We use multiple
43 types of geophysical observations to reliably image the subsurface. Our images of the subsurface
44 confirmed many findings from previous studies. The crust is thinner beneath New England, the
45 east coast, and the south-central United States. The interior of North America has a thicker crust.
46 The upper mantle seismic speed is slower beneath New England, the east coast, and the western
47 portion of the south-central United States. A smaller region of slower upper mantle speed in
48 Kentucky agrees with a published study, which linked the slower speed with a 75 Ma volcanic
49 site. We compared images of subsurface against earthquake locations. Earthquakes often locate
50 near regions with lateral subsurface structure changes. Lateral subsurface structure changes do
51 not always collocate with earthquakes. The type (faulting) of earthquakes weakly correlates with
52 the upper mantle seismic speed.

53 **1 Introduction**

54 The eastern United States (EUS) has a long and complex geological history that includes
55 at least two episodes of continental collision and breakup. The eastern part of North America
56 grew from the continent's Archean core through arc and continental collisions in the Early-
57 Middle Proterozoic (e.g., Whitmeyer, 2007). The resulting supercontinent Rodinia broke up
58 during the opening of the Iapetus Ocean in the Late Proterozoic (Hynes & Rivers, 2010).
59 Renewed plate convergence and episodic terrane accretion formed the supercontinent Pangea
60 during the Paleozoic and the early Mesozoic (e.g., Hatcher, 2010; Whitmeyer, 2007). The
61 opening of the Atlantic Ocean started in the Triassic-Jurassic (Hames et al., 2000). The east coast
62 became a passive margin around 180 Ma (Faill, 1998). Several stages of rifting modified the
63 passive margin (e.g., Whitmeyer, 2007). Except for first-order observations of a relatively fast

64 upper mantle, the relationship between the geological history and subsurface structure is still not
65 well known.

66 Though the EUS is naturally less seismically active than the western U.S., several
67 intraplate seismic zones (see Figure 1) including the New Madrid seismic zone (NMSZ), the
68 Wabash Valley seismic zone (WVSZ), the South Carolina seismic zone, the Central Virginia
69 seismic zone, and the West Quebec seismic zone (WQSZ) show localized seismic activity in the
70 east coast. Three great-to-major earthquakes (Magnitude 7-to-8) struck the NMSZ in 1811-1812
71 and caused severe damage (Hough et al., 2000; Johnston, 1996). Paleoseismic studies suggest
72 that at least two large earthquakes occurred thousands of years prior to 1800 (Tuttle, 2002). Past
73 destructive earthquakes and slow deformation (Newman, 1999) provoke debate over the seismic
74 hazard assessment (Stein, 2007). The mechanism of stress concentration that is proposed to have
75 caused these large events is unsolved. Some geodynamic models predicted a stress concentration
76 in the seismogenic zone (e.g., Levandowski et al., 2016; Pollitz, 2001). However, the assumed
77 structural models differ significantly due to poor images of the subsurface, especially in the
78 crust. Detailed structure images beneath the EUS are required to answer outstanding questions
79 such as what factors control the occurrence of intraplate earthquakes.



80

81 **Figure 1.** Seismicity (black and blue circles, magnitude 3 and larger prior May 2021 from the
82 USGS catalog) and cross-section locations (red lines). Black circles represent earthquakes that
83 are shown in cross-sections. Blue circles are earthquakes that are located 100 km away from any
84 cross-sections. The size of circles is proportion to magnitude. Abbreviations: CVSZ – Central
85 Virginia Seismic Zone; ETSZ – Eastern Tennessee Seismic Zone; NMSZ – New Madrid Seismic
86 Zone; OES – Oklahoma Earthquake Swarm; SCSZ – South Carolina Seismic Zone; WQSZ –
87 West Quebec Seismic Zone; WVSZ – Wabash Valley Seismic Zone. (For interpretation of the
88 references to color in this figure, the reader is referred to the web version of this article.)

89 The deployment of EarthScope USArray Transportable Array (TA) provided
90 unprecedented station coverage in the EUS for more than 10 years. The TA has crept

91 continuously across the U.S. and collected seismic observations at more than 2000 unique
92 locations. With a nearly uniform station spacing (~70 km) and high-quality sensors, the array
93 was designed to improve our understanding of subsurface structure and have led to many seismic
94 velocity models for the lithosphere structure of the EUS and surround regions (e.g., Biryol et al.,
95 2016; Bollmann et al., 2019; Dong & Menke, 2017; Golos et al., 2018; Menke et al., 2018; B.
96 Savage et al., 2017; Brian Savage, 2021; Wagner et al., 2018; B. B. Yang et al., 2014). To better
97 utilize the improved data coverage and compare the subsurface structure across a broad region,
98 we investigate the seismic velocity variations beneath the EUS with a model parameterization
99 that is suitable for TA stations.

100 Even with dense seismic networks, tightly constraining subsurface 3D geologic variations
101 is a challenge. But the seismological community has worked for decades with less data to extract
102 information valuable enough to steadily advance our understanding of the lithosphere. P-wave
103 receiver functions processed from teleseismic P-waves provide us a way to repeatedly sample
104 subsurface structure beneath seismic stations as source-side effects are removed by
105 deconvolution (e.g., Langston, 1979). To extract detailed subsurface structural parameters from
106 receiver functions, an inversion is often used to estimate model parameters from receiver
107 function observations. The inversion of receiver functions is non-unique (e.g., Ammon et al.,
108 1990), but incorporating complementary observations has shown to ease the non-unique problem
109 and improve the sensitivity (e.g., Chai et al., 2015; Chong et al., 2016; Julià et al., 2000, 2003;
110 Özalaybey et al., 1997; Sun et al., 2014). The construction of 3D models adds additional
111 complexity. Different data sets may average 3D heterogeneity differently, making one-
112 dimensional models that fit all the data difficult to construct. For example, 3D scattering in
113 receiver functions can introduce hard-to-identify high-wavenumber artifacts during an inversion.
114 An often used and generally successful approach to reduce these effects is to target smooth earth
115 models that represent averages of the true structure. We used the receiver function
116 smoothing/interpolation technique (Chai et al., 2015) to reduce the scattering noise in the data
117 prior to the inversion to avoid mapping noise into artifacts. Simultaneous inversion using
118 smoothed receiver functions has produced reliable images of subsurface seismic velocity
119 variations (Chai et al., 2015).

120 We simultaneously inverted smoothed/interpolated P-wave receiver functions, Rayleigh-
121 wave phase and group velocity measurements, and Bouguer gravity observations for subsurface
122 structure beneath the EUS using linearized uniform-cell-based 3D inversions. Compared with
123 recent studies (e.g., Porter et al., 2016; Schmandt et al., 2015; Shen & Ritzwoller, 2016), we used
124 a wider period range for surface-wave dispersion observations, included longer receiver function
125 signals, and reduced scattering noise in receiver functions through spatially smoothing. We
126 describe the procedures used to process each observation type in the next section. Details of the
127 receiver function smoothing/interpolation technique are discussed in the following section and
128 are followed with a description of the theory and processes for the simultaneous inversion. The
129 fits to each type of observations are illustrated in a separate section to show an important
130 component of the quality control applied to our results. We end with a discussion on the resulting
131 3D shear-wave velocity models that compares our results with recently published models and an
132 investigation of the relationship between seismicity and subsurface material variations.

133 2 Data

134 We used three types of geophysical observations to image the subsurface structure including P-
135 wave receiver functions, Rayleigh-wave dispersion measurements, and Bouguer gravity
136 observations. The receiver functions were computed using observations from about 1700 seismic
137 stations operated within the broad EUS (Figure S1).

138 2.1 Receiver function observations

139 P-wave receiver functions were processed using teleseismic waveforms recorded at TA,
140 and many other seismic networks (a complete list of networks can be found in Table S1).
141 Seismic events (around 3,700) with body-wave magnitude m_b larger than 5.7 during station
142 operation times (prior June 2015) and at epicentral distances from 30 to 100° (see Figure S2)
143 were selected to avoid P-waveform interference with upper mantle triplications and the core
144 shadow zone. We downloaded three-component P-waveforms along with metadata for these
145 events from the Data Management Center of Incorporated Research Institutions for Seismology
146 (IRIS DMC). The seismograms were rotated to the radial-transverse-vertical system from the
147 original north-east-vertical recording coordinates. P-wave receiver functions (Langston, 1979)
148 were obtained by deconvolving the vertical component from the radial and transverse
149 components using the time domain iterative deconvolution algorithm (Ligorria & Ammon,
150 1999). Gaussian filters (Ammon, 1991) were used in the deconvolution process to limit the
151 bandwidth of the receiver functions and preserve absolute amplitudes of receiver functions.
152 Specifically, we computed receiver functions with a Gaussian filter of 1.0 and 2.5 that
153 correspond roughly to pulse widths of 1.67 and 0.67 s at half the maximum, respectively.

154 Similar to receiver functions obtained for the western U.S region (e.g., Chai et al., 2015),
155 many receiver functions processed from even high-quality stations are quite noisy. In order to
156 exclude noisy outliers, we used three programmable waveform selection criteria. Other
157 waveform selection criteria have been used by previous studies (e.g., Yang et al., 2016), but
158 visual examinations of our receiver function waveforms confirm that these three criteria are
159 sufficient to remove problematic receiver functions from the data. First, receiver functions with
160 signal-to-noise ratios (measured using a 170 s time window that ends 10 s earlier than the
161 expected P arrival time as noise and a 130 s time window immediately after as signal) less than
162 10 were discarded. Second, since the deconvolution can be unstable, we reject receiver functions
163 with convolution fit less than 85%; the convolution fit is computed as a signal power ratio
164 between the radial component and a convolved signal of receiver function and the vertical
165 component. Even with these relatively strict criteria, occasionally, some problematic receiver
166 functions (e.g. unusual large amplitude, wrong polarity, low-frequency noise) could pass through
167 and influence our observations. To identify these signals, we computed the signal difference of
168 each receiver function with respect to the single-station averaged waveform to further clean up
169 our receiver function data set and excluded receiver functions with signal difference larger than
170 300% of the stacked waveform signal power. The distribution of receiver function signal
171 differences follows the extreme value distribution for the EUS data set (Figure S3), which
172 suggests a small portion of receiver functions is significantly different from the single-station
173 averaged receiver functions. We obtained around 228,000 (38% of the raw receiver functions)
174 acceptable receiver functions in total. The accepted receiver functions were then binned into
175 three ray parameter bins (smaller than 0.05 s/km, larger than 0.07 s/km and in between) for both

176 Gaussian 1.0 and 2.5 receiver functions. Therefore, we have six receiver function waveforms at
 177 station when data are abundant.

178 2.2 Surface-wave dispersion observations

179 We used both Rayleigh wave group and phase velocity observations in the simultaneous
 180 inversion. We avoid Love waves to minimize complexity that may arise from anisotropy. Our
 181 results are thus an approximation of the potentially anisotropic Earth. Surface-wave dispersion
 182 observations from two studies were blended to combine the short period dispersion values from
 183 Herrmann et al. (2021) and longer period dispersion observations from Ekström (2011). The
 184 short period dispersion observations were measured using both earthquake signals and ambient
 185 noise cross-correlations. The measured dispersion observations were localized to grid points
 186 through a surface wave tomography (e.g., Ekström, 2011; Herrmann et al., 2021). The short
 187 period dispersion model used a 1°-by-1° grid with a node at the center of each grid cell. Only the
 188 dispersion data corresponding to cells with good ray path coverage (at least 50 km of ray path)
 189 were used. We adopted the following formula from Maceira & Ammon (2009) for a smooth
 190 blending of the dispersion curves.

$$191 \quad s(T) = \cos^2 \varphi s_2(T) + \sin^2 \varphi s_1(T) \quad (1)$$

192 in which

$$193 \quad \varphi = \frac{\pi}{2} \frac{1 + \tanh[\varepsilon(T - T_c)]}{2}$$

194 In the expressions above, $s(T)$ is the blended dispersion value (group or phase velocity). T
 195 is the period, $s_1(T)$ is a value from the long-period dispersion tomography (Ekström, 2011), and
 196 $s_2(T)$ is a value from the short-period dispersion tomography (Herrmann et al., 2021) at the same
 197 period. φ is a control parameter that is a function of T_c and ε . ε is set equal to 0.5. T_c is the period
 198 around which we want to switch from short- and long-period surface wave observations. Since
 199 the available period range varies from location to location (due to ray path coverage differences),
 200 we used a grid search to determine the best transitional period (T_c). We tried a range of T_c and
 201 computed the gradient of the resulting dispersion curves. In order to minimize artificial
 202 anomalies caused by the blending, the optimal T_c is the one with a minimum gradient (the
 203 smoothest dispersion curve). All blended dispersion curves were visually examined and minor
 204 adjustments were made as needed. Generally, a dispersion-curve transition period between 30-40
 205 s was chosen. The blended dispersion data set spans from 3 s to 250 s in the best case. As an
 206 example, the blended dispersion curves are compared with recent dispersion models (Bensen et
 207 al., 2007; Ekström, 2011, 2014; Herrmann et al., 2021; Jin & Gaherty, 2015) in Figure S4. The
 208 blending of dispersion curves greatly extended the period range and are consistent with
 209 alternative recent dispersion models at most places.

210 2.3 Gravity observations

211 Gravity observations were extracted from a global Bouguer gravity model WGM2012
 212 (Balmino et al., 2012). This Bouguer gravity data set was computed by spherical harmonic
 213 analysis using ETOPO1 topography-bathymetry data and gravity observations from the
 214 EGM2008 global gravity model (Pavlis et al., 2012). The lateral resolution of the gravity data is
 215 5 arc minutes (~9 km), which is higher than what we can resolve with a 1°-by-1° grid in our
 216 inversion. The Bouguer gravity observations are averaged within a 1°-by-1° grid for the EUS to
 217 reduce gravity anomalies that are due to smaller-scale structure perturbations. Long wavenumber

218 gravity signals are primarily caused by deep density changes. However, interpretation of deep
 219 gravity signals is nonunique and can be associated with density variations, plate flexure, and
 220 upper mantle dynamic effects. We wavenumber filtered the gravity observations with a box-car
 221 filter so that the remaining gravity signals are mainly sensitive to the shallow density structure
 222 (upper ~15 km). Initial gravity observations from WGM2012 and wavenumber filtered gravity
 223 values are compared in Figure S5. The filtered gravity image shows fewer small scale and large
 224 wave-number variations than the raw image as expected.

225 **3 Receiver-function smoothing/interpolation**

226 P-wave receiver functions and surface-wave dispersion observations have different
 227 spatial (lateral) sensitivity. Receiver functions are sensitive to sharp changes in vertical and
 228 lateral structure. In particular, large, complicated (and hopelessly aliased) variations near the
 229 surface often strongly influence P-wave receiver functions. Surface-wave dispersion
 230 observations are more sensitive to longer wavenumber variations in the structure. We smoothed
 231 the receiver-function wavefield spatially to reduce near-surface scattering effects and to better
 232 complement the surface-wave dispersion measurements. We have developed receiver function
 233 smoothing/interpolation to attack this issue by simplifying the receiver function wavefield (Chai
 234 et al., 2015). The smoothing/interpolation reduces the scattering noise on receiver function
 235 observations and isolates the spatially coherent components of the signals (see Figure 2 and
 236 Figure S6). Compared with the traditional single-station-averaged receiver functions,
 237 interpolated/smoothed receiver functions are more consistent laterally for different lag times.

238 A spatially smoothed receiver function is computed by averaging receiver functions
 239 recorded at adjacent stations with distance-dependent weights. Smoothing/interpolation also
 240 equalizes the lateral sensitivity of receiver functions and surface-wave dispersion measurements,
 241 which can reduce potential inconsistencies between surface-wave observations and body-wave
 242 receiver functions. Interpolation also provides us a way to approximate receiver functions at grid
 243 points where surface-wave observations are commonly estimated by tomography. This
 244 functionality is quite useful especially for 3D inversions using multiple types of observations.
 245 We can express the receiver function wavefield as $R(x,y,t)$, where x and y are spatial coordinates
 246 (e.g. latitude and longitude), and t is lag time after the direct P wave. Then, the interpolated
 247 receiver function wavefield is computed using the following formula repeatedly for all locations
 248 of interest (e.g. grid points)

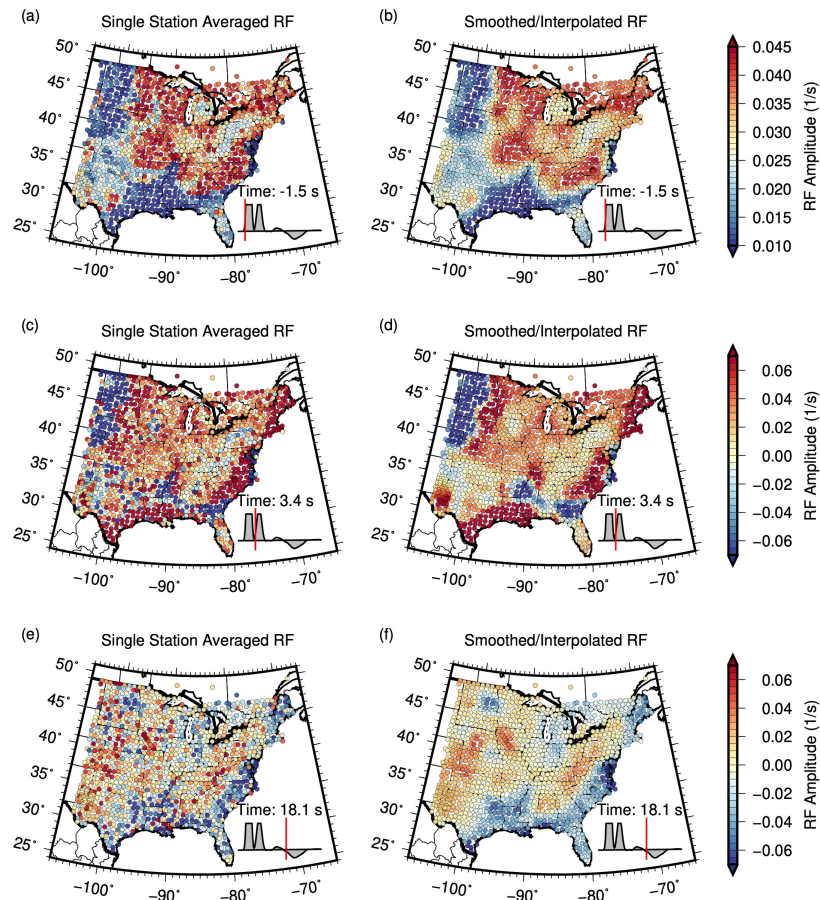
$$249 \quad R_i(x_i, y_i, t) = \frac{\sum_{j=1}^n \omega_j R_j(x_j, y_j, t)}{\sum_{j=1}^n \omega_j}$$

250 with

$$251 \quad \omega_j = \begin{cases} 1 & \text{if } r_{ij} < d_1 \\ \frac{r_{ij} - d_1}{d_1 - d_2} + 1 & \text{if } d_1 < r_{ij} < d_2 \\ 0 & \text{if } r_{ij} > d_2 \end{cases}$$

252 where r_{ij} is the distance between the point of interest (x_i, y_i) and station location (x_j, y_j),
 253 and n is total number of stations. d_1 and d_2 ($d_1 < d_2$) are two distance parameters that control the
 254 distance range for the stations included in the averaging and the weight (ω_j) of the different
 255 stations. Receiver functions recorded at stations at distances less than or equal to d_1 are weighted

256 as 1. Stations located at distances between d_1 and d_2 are weighted between 0 and 1 with the
 257 weight linearly decreased from 1 at distance d_1 to 0 at distance d_2 . Chai et al. (2015) compared
 258 smoothed receiver functions computed using several pairs of distance parameters for different
 259 seismic network configurations in the western U.S. In our analysis, we choose a d_1 of 110 km
 260 and a d_2 of 160 km for the EUS to match the 1° grid used for surface-wave dispersion
 261 tomography. By spatially smoothing the receiver function wavefield, we sacrifice spatial
 262 resolution for simplicity and better average properties, but we may blur some geological
 263 transitions and boundaries. The resulting smoothed receiver functions are more complementary
 264 to the surface-wave dispersion data and comprise a data set more consistent with the other
 265 observations used in the joint inversion and with less near-surface scattering effects that can
 266 complicate the inverse models.



267

268 **Figure 2.** Time slice at time -1.5 s (a, b), 3.4 s (c, d) and 18.1 s (e, f) from receiver function
 269 wavefield in the EUS and adjacent Canada. Each circle represents a seismic station at which we
 270 have computed a stacked receiver function. The color indicates the amplitude of (a, c, e) the
 271 receiver function averaged at each station or (b, d, f) the smoothed/interpolated value of the
 272 receiver function wavefield. Inset shows the stack of all RFs (clipped to show details), and the
 273 red line shows the corresponding lag time of the time slice. See Movie S1 for all the time slices.
 274 (For interpretation of the references to color in this figure, the reader is referred to the web
 275 version of this article.)

276

277 **4 Simultaneous inversion**

278 To estimate the subsurface shear wave speeds beneath the EUS, we simultaneously
 279 inverted the smoothed/interpolated receiver function wavefield, Rayleigh wave group and phase
 280 velocities in the period range from 3 to 250 s, and wavenumber-filtered Bouguer gravity
 281 observations. The study region was divided into 950 1°-by-1° size cells for the EUS so the best
 282 lateral resolution of our model is 110 km by 110 km. The resulting 3D grid was used for our
 283 simultaneous inversions in a hybrid 1D-3D manner. Receiver-function and surface-wave-
 284 dispersion calculations were performed with a 1D formalism for each cell across the region
 285 where observations are available. Gravity calculations were computed in 3D using rectangular
 286 prisms. The lateral dimension of the prisms is the same as the grid size whereas the vertical
 287 dimension varies from 1 km near the surface to 50 km in the mantle. A linearized discrete
 288 geophysical inversion developed from (Chai et al., 2015; Julià et al., 2000; Maceira & Ammon,
 289 2009) was used with smoothness-based stabilization. A jumping strategy is used for
 290 regularization to allow constraints directly on model parameters, not changes in model
 291 parameters (e.g., Constable et al., 1987). The linearized inversion can be expressed as

$$292 \begin{pmatrix} \sqrt{\frac{p(T)}{\omega_s^2}} D_s \\ \sqrt{\frac{1}{\omega_r^2}} D_r \\ \sqrt{\frac{1}{\omega_g^2}} D_g \\ \eta \Delta \\ W \\ S \end{pmatrix} m_1 = \begin{pmatrix} \sqrt{\frac{p(T)}{\omega_s^2}} R_s \\ \sqrt{\frac{1}{\omega_r^2}} R_r \\ \sqrt{\frac{1}{\omega_g^2}} R_g \\ 0 \\ 0 \\ 0 \end{pmatrix} + \begin{pmatrix} \sqrt{\frac{p(T)}{\omega_s^2}} D_s \\ \sqrt{\frac{1}{\omega_r^2}} D_r \\ \sqrt{\frac{1}{\omega_g^2}} D_g \\ 0 \\ 0 \\ 0 \end{pmatrix} m_0 + \begin{pmatrix} 0 \\ 0 \\ 0 \\ 0 \\ W \\ 0 \end{pmatrix} m_a$$

293 where D_s , D_r and D_g are matrices containing the partial derivatives of the seismic shear velocity
 294 model corresponding to the dispersion, receiver function, and gravity estimates, respectively. m_0
 295 is the 3D velocity model from previous iteration. m_a is the a priori velocity model. m_1 is the
 296 updated velocity model for the current iteration. R_s , R_r and R_g are the corresponding data residual
 297 vectors, and ω_s^2 , ω_r^2 and ω_g^2 are global weights assigned to the three data sets. Those weights are
 298 defined in the same way as Julià et al. (2000) as $N\sigma_k^2$ where N is the number of data points for
 299 the specific data set and σ_k^2 is the k th data point variance. $p(T)$ was introduced by Maceira &
 300 Ammon (2009) to control the trade-off between fitting both gravity and surface-wave dispersion
 301 measurements. The matrix Δ applies vertical smoothing with a weight η to make the 1D velocity
 302 profiles vary smoothly - necessary when data constraints are not sufficient. W is a diagonal
 303 matrix to constrain the velocities from varying too far from the a priori values in m_a with
 304 associated weights. Lateral smoothing is added through the matrix S using the first differences
 305 between shear velocity values in adjacent grid cells. The lateral smoothing does not smooth
 306 across the ocean-continent boundary to allow a sharp change in material properties across this
 307 well-defined (for our cell size) feature. The inverse equation is solved using a Conjugate-
 308 Gradient LSQR solver for sparse linear equations (Paige & Saunders, 1982). The weights and
 309 smoothing parameters are determined by performing suites of inversions and comparing data
 310 misfits and model properties such as roughness. Interactive visualization tools were used to help
 311 the comparison of inversion results with different weighting parameters (Chai et al. 2018). The
 312 vertical smoothness constraints increase with depth to reflect a loss in data resolution and the

313 increase in surface wavelengths sampling the greater depth in the model. Partial derivatives for
314 surface wave dispersion were computed using finite-difference approximations. The simulation
315 of surface-wave dispersion is based on algorithms from Saito (1988). The gravity derivatives
316 were computed using the equations from Plouff (1976) and the chain rule. The inversion is
317 performed to estimate shear-wave speed, which is related to P-wave speed by the V_p/V_s ratio,
318 and to the density using formulas described in Maceira & Ammon (2009) and Chai et al. (2015).
319 The V_p/V_s ratio was fixed throughout the inversion (inherited from the initial model).

320 The inversion for the EUS started with an initial model that was based on Crust Model
321 1.0 (Laske et al., 2013). Velocities below the crust were initialized with the AK135 velocity
322 model (Kennett et al., 1995). Since flat-Earth codes were used to compute dispersion, the initial
323 model was flattened using the formulas from Biswas (1972) with a slightly modified density
324 transformation exponent (see the supplements of Chai et al., 2015 for details). Velocities and
325 densities were unflattened prior to the gravity partial calculation and flattened after the gravity
326 computation since the density-shear velocity relationship is based on laboratory measurements
327 (corresponding to the spherical model).

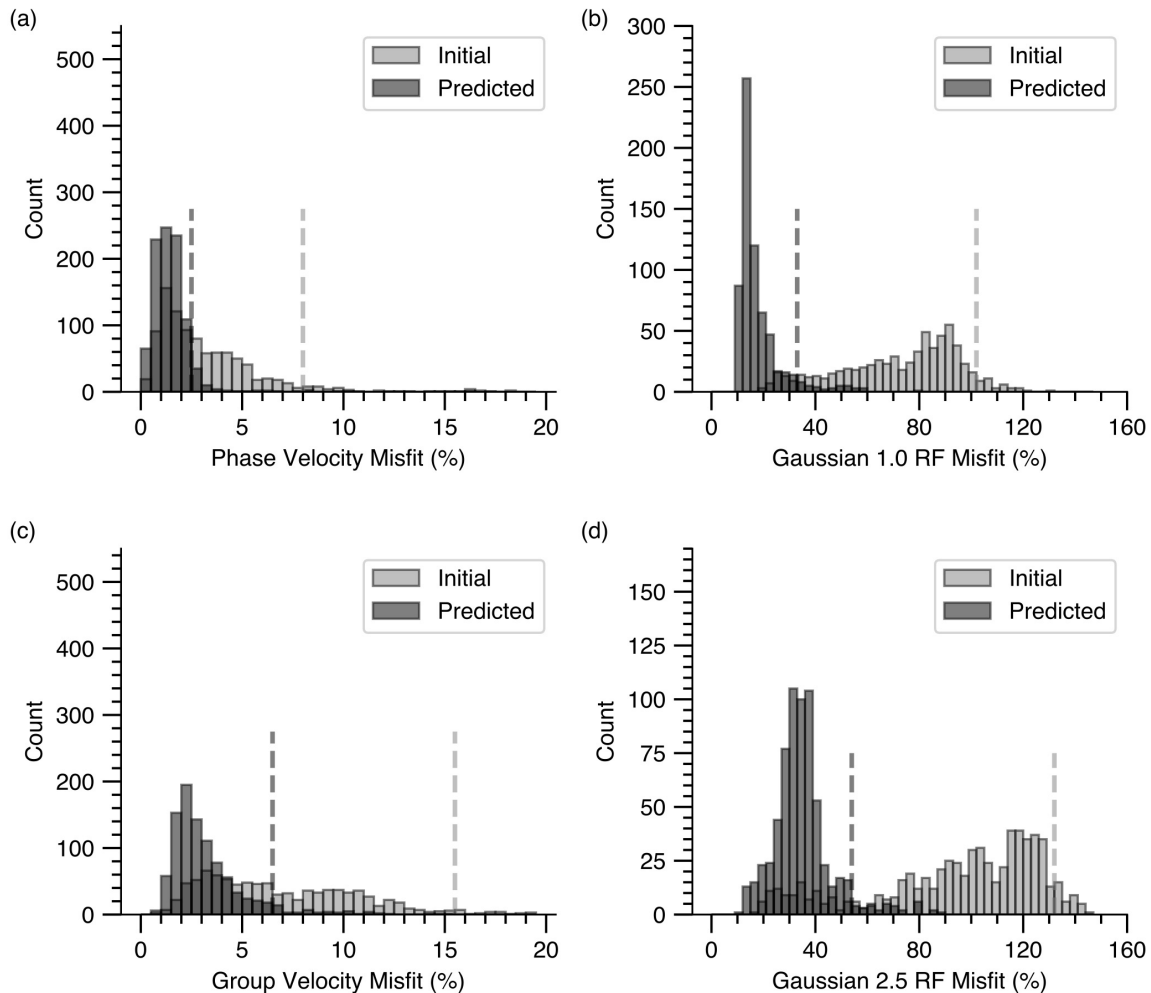
328 Based on the results from hundreds of 3D inversions (multiple cells) and thousands of 1D
329 inversions (single cell), it became clear that tuning the weights for each data set and constraints
330 is necessary to produce good fits to the observations. We experimented with weight selection
331 using numerous 1D inversions with observations selected from several samples in the overall
332 data set. We searched for optimal ranges of weight parameters by randomly testing 1D inversion
333 parameters, and examining the range of velocity models that resulted from the simulation.
334 Within this suite of velocity models, some fit the data poorly. For many choices of the weights,
335 the results were quite similar - those that fit the observations well often differed from the average
336 model by less than 0.1 km/s. The tests suggest we can use data fits as a guide to select both the
337 data and smoothness weights for the larger 3D inversions. To be sure that the resulting model fits
338 the observations reasonably well, we used interactive visualization tools (Chai et al., 2018) to
339 visually check data fits for all three types of observations.

340 The EUS results were obtained after eight total iterations of the 3D inversion (Figure S7).
341 We began the inversion without gravity observations and modeled the seismic data for a total of
342 four iterations. We then added the gravity observations for the final four iterations. The final
343 EUS model has been unflattened for interpretation and easy comparison with published spherical
344 Earth models.

345 **5 Data fits**

346 Fitting data is the most important quality control for our inversion. We discuss not only
347 the overall data fit of the three types of observations we use but also the spatial distribution of
348 data misfits. Fit to surface-wave dispersion and receiver functions is significantly improved in
349 the first four iterations and are stable for the last four iterations (Figure S7). Gravity misfit was
350 reduced greatly after one iteration. In general, our inverted model fits all three types of
351 observations much better than the starting model. Figure 3 shows the receiver function and
352 surface-wave dispersion misfit distributions of all cells for the initial and final models. In all
353 cases, an improvement in fit is clear. We use a 95% threshold to quantify the overall misfit. The
354 95% misfit threshold represents the fractional misfit value equal to or larger than that found for
355 95% of the cells. The metric is used to eliminate the influence of the worst fitting 5% of the cells
356 (which are often in the ocean, where data coverage is substantially more limited). As shown in

357 Figure 3, the 95% misfit threshold was improved from 15.5% (initial model) to 6.5% (inverted model) for
 358 group-velocity measurements, from 8% (initial model) to 2.5% (inverted model) for
 359 phase-velocity measurements, from 102% (initial model) to 33% (inverted model) for Gaussian
 360 1.0 receiver functions, and from 132% (initial model) to 54% (inverted model) for Gaussian 2.5
 361 receiver functions. The modest reduction in dispersion misfits reflects the relatively small range
 362 of speeds within the data. Any model with a roughly correct average dispersion value performs
 363 reasonably well with this metric. As expected, phase-velocity measurements are fit better than
 364 group-velocity measurements. Narrowband receiver functions were fit better than broadband
 365 receiver functions.



366

367 **Figure 3.** Comparison of misfit using the initial model (lighter color) and the inverted model
 368 (darker color) for (a) phase velocity, (b) Gaussian 1.0 receiver functions, (c) group velocity, and
 369 (d) Gaussian 2.5 receiver functions. Dashed lines show the misfit value that is larger than misfits
 370 for 95% of measurements. A root-mean-squared (RMS) misfit is normalized with the RMS of
 371 the corresponding observation.
 372

373 5.1 Receiver function misfits

374 In Figure S8, we show the spatial distribution (at available grid points) of receiver
375 function misfits for both the initial model and the inverted (final) model. Receiver function
376 misfits computed from the initial model are quite large at most grid points. The misfit shown in
377 the maps (Figure S8a and b) is the average of those corresponding to all available (up to six)
378 receiver functions. For example, at the location corresponding to Figure S8c, the misfit
379 (represented as the circle size in Figure S8a and b) is computed from six receiver functions (three
380 ray parameter bins and two Gaussian widths). Comparing the observed and predicted receiver
381 functions in Figure S8c, we found the converted phase and multiples arrive later in initial-model
382 receiver functions. Receiver functions computed from the inverted model agree well with
383 observations. At many grid points, the receiver functions computed with the initial model differ
384 significantly from the observations, while the inverted model fit the observations nicely (see
385 Figure S8d for an example). Receiver function misfits corresponding to the inverted model are
386 uniformly small with slightly larger values in Gulf of Mexico coastal regions and the Williston
387 basin where thick sediments complicate receiver function waveforms. The relatively large misfits
388 in the eastern Tennessee and western North Carolina may due to anisotropy or less-optimal
389 V_p/V_s ratios.

390 5.2 Surface-wave dispersion misfits

391 The spatial distribution of surface-wave dispersion misfits (an average of group and
392 phase speed misfits) is shown in Figure S9. Group and phase velocities computed from the initial
393 model differ significantly from surface-wave dispersion observations for most model grid points
394 as indicated by cells with large circles in Figure S9a. For example, we compared observed and
395 simulated dispersion curves at a grid point located in northeast Mississippi in Figure S9c.
396 Predicted dispersion curves based on the inverted model agree well with the observations while
397 simulated group and phase velocities from the initial model are too small at most periods. Even
398 for regions that the initial-model-derived surface-wave dispersion curves are similar to
399 observations (see Figure S9d for an example), the inverted model predicts the surface-wave
400 measurements better, especially at short periods (less than 20 s). As shown in Figure S9c,
401 surface-wave dispersion misfits corresponding to the inverted model are much smaller than those
402 from the initial model except for a few off-coast locations. Large misfits at these off-coast grid
403 points (at the gulf coast of Florida and near northern New Jersey) are likely due to limited
404 observations and a poor starting model.

405 5.3 Gravity misfits

406 Gravity observations are much fewer in number compared to receiver functions and
407 surface-wave dispersion. For this reason, we use a smaller weight for gravity observations and
408 include gravity data at a later stage of the inversion. The predicted gravity values agree with
409 Bouguer gravity observations well (Figure S10). Since the gravity calculations are performed in
410 3D, we used a buffer zone (gray color filled regions in Figure S10) to avoid edge effects. In
411 general, our goal with the gravity data is to fit the relatively high-wavenumber features that are
412 likely associated with crustal density variations. The addition of gravity to the inversion does not
413 introduce significant changes to the model. However, these changes are necessary to fit the
414 gravity observations. Numerical tests showed that small changes of roughly 0.1 km/s to the upper

415 15 km account for an improved fit to the gravity. We only fit the first-order features in gravity
416 observations to avoid overfitting.

417 **6 Results**

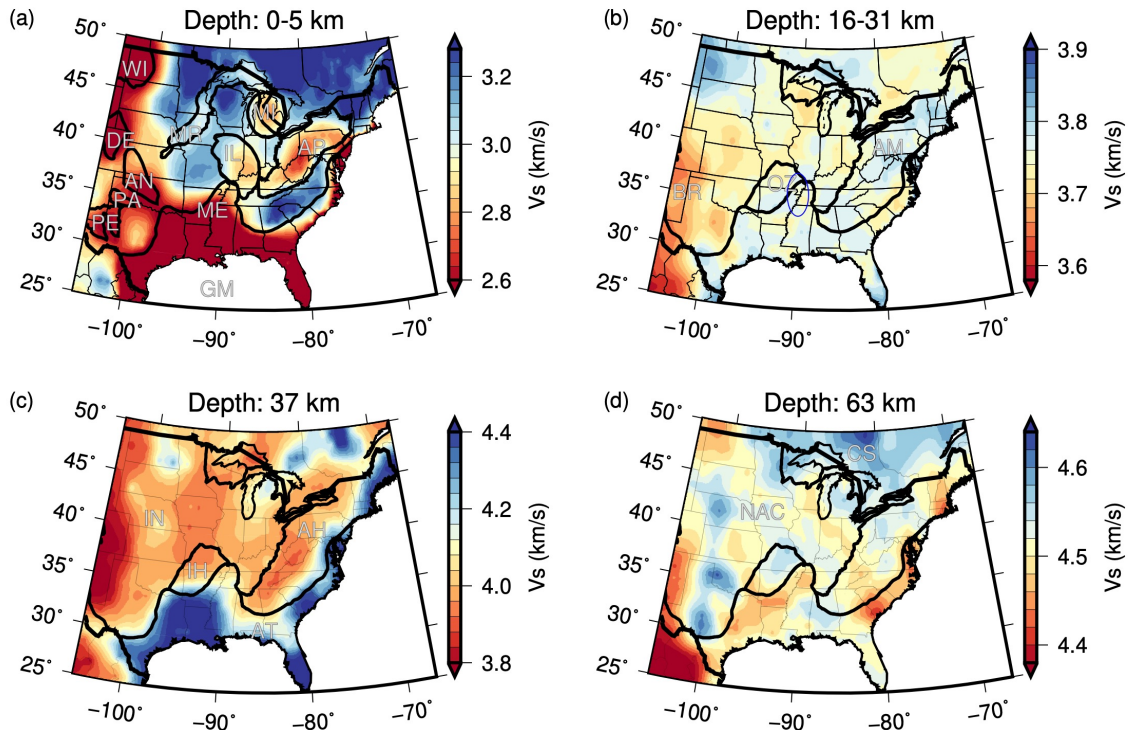
418 Representative shear-velocity depth slices are shown in Figure 4. Maps in Figure 4a-b are
419 a plot of the average speed within the specified depth range. At shallow depth (0-5 km, Figure
420 4a), low velocities correlate well with major sedimentary basins and the coastal plains. Low
421 velocity layers near the surface are thick along the coastal plains and within the basins of the
422 Great Plains, compared with the Michigan, Illinois, and Appalachian basins. Average lower
423 upper-crustal shear velocities are lower beneath the Mid-continent rift, which interrupts the
424 relatively fast shallow crusts of Wisconsin and northern Minnesota and the Canadian Shield
425 regions to the north and continues southward through southern Minnesota and Iowa. There is a
426 hint (solid ellipse in Figure 4b) of a sharper transition along the northern (western) Mississippi
427 Embayment (ME) boundary than along the east. Seismicity extends from the lower shear wave
428 speeds into a region of more normal speeds. On average, the Appalachian region and the
429 Midwest appear slightly faster than the region to the west that includes Wisconsin, Iowa,
430 Nebraska, Kansas, and Oklahoma. The fast region in the northwest lies beneath the Williston
431 Basin and is not well resolved, but the model, driven by dispersion measurements at these
432 depths, suggests perhaps an unusually fast middle crust beneath the basin (Figure 4b). Two east-
433 coast regions, the Carolinas and southern Virginia, and Maine appear slower than regions
434 immediately west in the middle crust (Figure 4b).

435 Figure 4c is a map of the shear-velocity model at 37 km depth. This depth was chosen to
436 provide first-order information on crustal thickness - in areas of thin crust, we see mantle-like
437 speeds (dark blue colors, V_s larger than 4.4 km/s), while in many other areas, we simply see the
438 lower crust. The map identifies the southern ME and coastal regions as regions of unusually thin
439 crust. Regions of relatively fast deep crust are suggested in the eastern Dakotas, beneath
440 Michigan, and parts of Canada and New England (see Figure 5 for crust thickness variations).
441 We discuss specific estimates of crustal thickness later. Figure 4d is a map of the shear-wave
442 model at a depth of 63 km, which provides a sample of the shear-wave speeds in the uppermost
443 mantle. The range of velocity variation is about 6%. The image indicates a relatively slower
444 upper mantle along the east coast from New England to South Carolina. A low velocity feature
445 extends from the northern ME south to Louisiana and east Texas. The fastest speeds are to the
446 north, into the Canadian Shield region.

447 Figure 5 includes a crustal thickness map along with example velocity profiles that were
448 extracted from the model. Example velocity profiles at eight different locations (Figure 5a-d, f-i)
449 show detailed velocity changes as a function of depth. To define crustal thickness, we measured
450 the depth corresponding to P-wave velocity larger than 7.8 km/s (based on visual inspections of
451 velocity profiles). Only a few cells failed to reach this speed before a depth of 53 km. The
452 automatically measured crustal thicknesses are shown as dashed gray lines in Figure 5a-d,f-i,
453 which match the crust-mantle transition well visually at all presented locations.

454 Our smoothing approach to receiver functions and reliance on surface-wave dispersion
455 tomography to constrain the deeper features in the model increase the consequences of the
456 assumption of sharp features such as the crust-mantle boundary in the initial model (Crust 1.0)
457 on the location of the crust-mantle transition. However, as shown earlier, even when the model is
458 good, slight adjustments are made to improve the alignment of the converted phases originating

459 from the crust-mantle boundary region. Although we did not perform a rigorous analysis, our
 460 examination of the model suggests that when the constraints used to build Crust 1.0 were based
 461 on good nearby data, little adjustment in crustal thickness was needed by our inversion. In
 462 regions where we believe that Crust 1.0 relied heavily on interpolation, the inversion changes
 463 from our initial model were larger. Although adjustments are generally not large, typically 3 km,
 464 our model is almost systematically thinner than Crust 1.0 by a few kilometers (both models share
 465 the same V_p/V_s ratio).

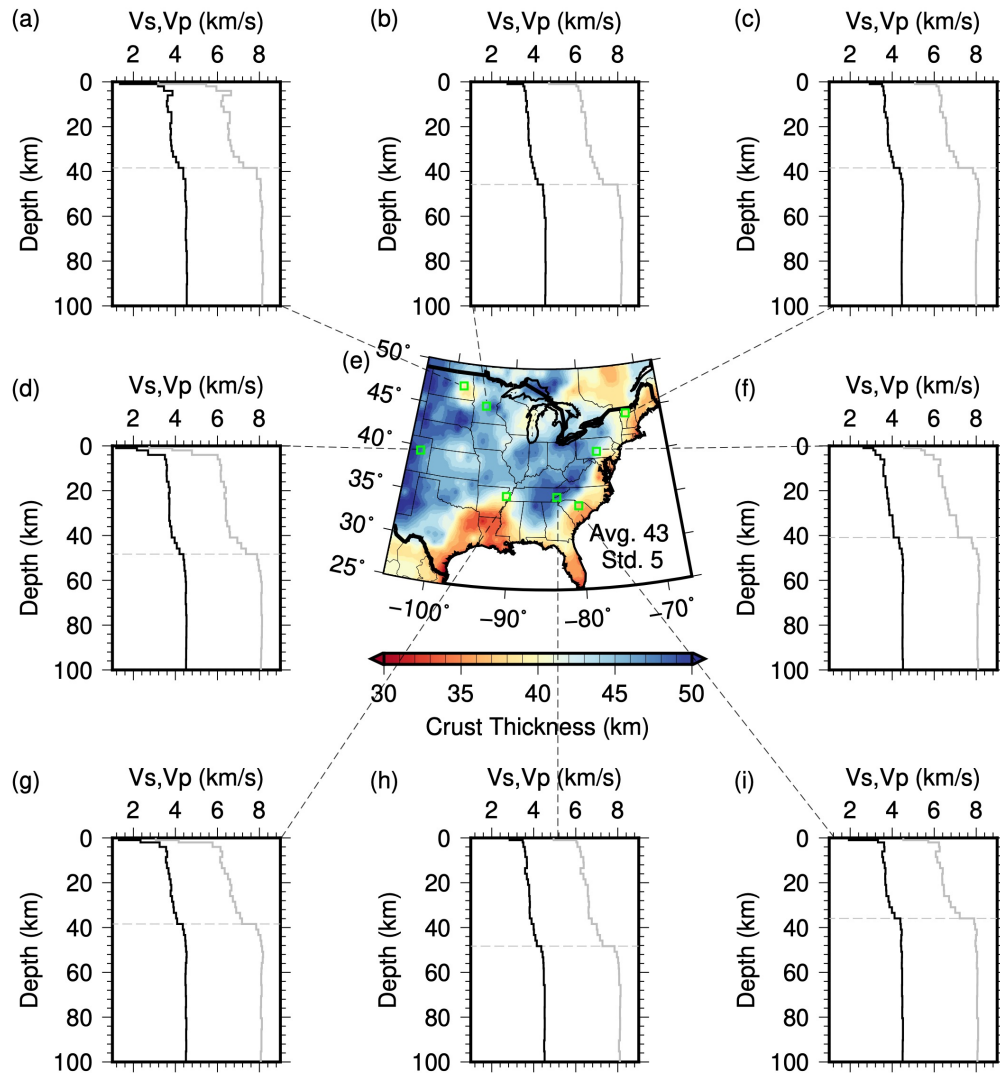


466

467 **Figure 4.** Shear-velocity maps showing depth range (a) 0-5 km, (b) 15-31 km, (c) 37 km, and (d)
 468 63 km from the 3D model. Thick black lines in (a) indicate major sedimentary units. Thick black
 469 lines in (b), (c) and (d) show the physiographic boundaries. Thin black lines show state
 470 boundaries. Warm colors show relatively slower regions, cool colors indicate relatively faster
 471 regions. Although the colors are constant, the velocity range in each figure varies substantially.
 472 The anomalies at 0-5 km depth are primarily corresponding to sedimentary basins. The velocity
 473 changes at 15-31 km depth are related to lateral variations in mid-lower crust structure.
 474 Abbreviations: AH – Appalachian Highlands; AM – Appalachian Mountains; AN – Anadarko
 475 Basin; AP – Appalachian Basin; AT – Atlantic and Gulf Coastal Plains; BR – Basin and Range;
 476 CS – Canadian Shield; DE – Denver Basin; GM – Gulf of Mexico; IH – Interior Highlands; IL –
 477 Illinois Basin; IN – Interior Plains; ME – Mississippi Embayment; MI – Michigan Basin; MR –
 478 Midcontinent Rift; NAC – North America craton; OZ – Ozark Uplift; PA – Palo Duro Basin; PE
 479 – Permian Basin; WI – Williston Basin. (For interpretation of the references to color in this
 480 figure, the reader is referred to the web version of this article.)

481 Crustal thickness patterns for eastern North America are familiar. The crust is thinner
 482 near the coast and thicker landward. The average crustal thickness in the region is 43 km with a
 483 standard deviation of 5 km. Relatively thinner crust (< 43 km) is also imaged beneath eastern

484 North Dakota. The crust beneath the ME and into east Texas appears significantly thinner (< 35
 485 km) than the continental interior. Thicker crust (> 43 km) is found beneath the Appalachian
 486 Mountains and the Great Plains. The depth of the crustal-mantle transition is less well
 487 constrained beneath thick sedimentary basins due to the dominance of basin reverberations in the
 488 receiver functions. One potential application of our model is to form the basis of a wavefield
 489 downward continuation and decomposition (Chai et al., 2017; Langston, 2011) to extract
 490 receiver function signals generated from the crust-mantle transition from teleseismic P-wave
 491 seismograms assuming the shallow structure is known. We leave that analysis for future efforts.



492

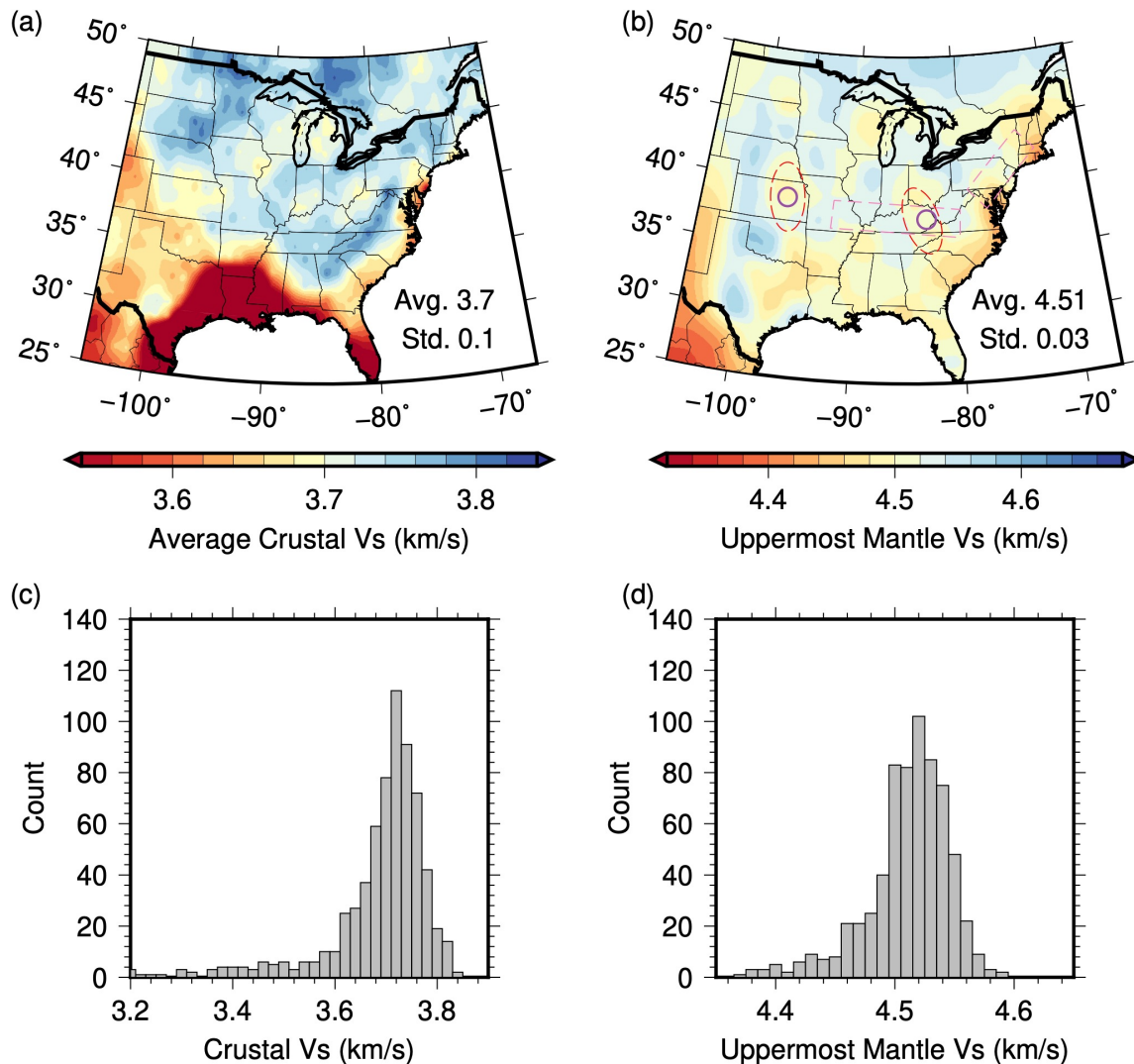
493 **Figure 5.** Crustal thickness map of (e) the EUS and (a-d, f-i) example velocity profiles at eight
 494 locations. Warm colors show relatively thinner crust, cool colors indicate relatively thicker crust.
 495 The average crustal thickness is 43 km with a standard deviation of 5 km. Green boxes on the
 496 map show the location of the corresponding velocity profile. In the profile plots (a-d, f-i), black
 497 lines represent shear-wave velocity while gray lines correspond to P-wave velocity. The dashed
 498 gray lines indicate the measured crustal thickness. (For interpretation of the references to color in
 499 this figure, the reader is referred to the web version of this article.)

500

501 We compared our crustal thickness measurements with several published models
502 (Crotwell & Owens, 2005; Porter et al., 2016; Schmandt et al., 2015; Shen & Ritzwoller, 2016).
503 The EARS (Crotwell & Owens, 2005) project measured crustal thickness from automatically
504 computed P-wave receiver functions using H-k stacking method (Zhu & Kanamori, 2000) by
505 assuming a constant velocity in the crust. The original results may suffer from scattering noise in
506 receiver functions (e.g., Chai et al., 2015). We spatially smoothed the measured crustal thickness
507 from EARS to show first-order features (see Figure S11). Comparing our crustal thickness map
508 (Figure 5a) with four recently published models (Figure S12), we note that a thinner crust was
509 imaged along the east coast and beneath the ME for all models. However, notable differences
510 exist among these models. The average crustal thicknesses and the standard deviations from the
511 Shen-2016 model (Shen & Ritzwoller, 2016), the Schmandt-2014 model (Schmandt et al., 2015),
512 and our model are the same. The EARS model (Crotwell & Owens, 2005) may underestimate
513 crustal thicknesses due to oversimplified model parameterization (constant-velocity crustal
514 layer). The Porter-2015 model (Porter et al., 2016) used the EARS results to constrain crustal
515 thickness and shared the same issue. The common conversion point (CCP) stacking procedure
516 (Zhu, 2000) used for the Schmandt-2014 model reduced some scattering but had difficulty in
517 challenging regions (sedimentary basins for example) where stacking energy is not focused. To a
518 large degree, the Schmandt-2014 model, the Shen-2016 and our model are consistent. Small
519 differences exist between the Shen-2016 and our model (see Figure S13). The EARS model is
520 certainly suitable for a starting model. We believe that our model is less contaminated by
521 scattering in receiver functions and includes simultaneously-modeled constraints from Rayleigh
522 waves (similar to the Shen-2016 model) and near-surface gravity.

523 Figure 6a and b are maps of the average crustal and upper-mantle shear-wave speed,
524 respectively. The mean of the average crustal V_s velocity across the model continental grid
525 points is 3.7 km/s (standard deviation 0.1 km/s). The corresponding mean crustal V_p velocity is
526 6.5 km/s (standard deviation 0.2 km/s, see Figure S14). These mean values agree reasonably well
527 with the global compilation of Christensen & Mooney (1995). Relatively fast average crustal
528 velocity is found beneath the stable North America craton. Regions of very slow average crustal
529 shear-wave speeds are associated with thick sediments in the southern ME. The mean uppermost
530 mantle shear-wave speed is the average of the upper 60 km of the mantle and it is 4.50 km/s
531 (standard deviation 0.05 km/s). The average uppermost mantle P-wave speed in the study area is
532 8.1 km/s (standard deviation 0.1 km/s), which is also consistent with the global compilation
533 (Christensen & Mooney, 1995) and regional surveys (Li et al., 2007). Note these P-wave speeds
534 were derived from shear-wave speed using V_p/V_s ratios inherited from Crust 1.0. The uppermost
535 mantle shear-wave velocity is slowest beneath New Mexico and the associated southern Basin
536 and Range province. We imaged relatively slow average shear-wave speeds in the uppermost
537 mantle beneath New England and the southeastern US, regions that may have interacted with
538 Great Meteor (e.g., Eaton & Frederiksen, 2007) and Bermuda (e.g., Cox & Van Arsdale, 2002)
539 hotspots respectively. Slow speeds along the east coast seem to follow the trend of eastern North
540 America rift basins but extend further into northern New England than the surface expression of
541 rifting. A slightly slower uppermost mantle is imaged beneath the western ME. Localized low
542 average mantle speeds (dashed ellipses in Figure 6b) near the Kansas-Nebraska border and the
543 Kentucky-Ohio border are situated near kimberlite volcanic site and may represent modified
544 lithosphere associated with these volcanic structures. The relatively slow upper mantle weakly
545 correlates with the region of thrust faulting along the eastern margin of the U.S. and within

546 southeast Canada. The thrust faulting environment also correlates with the thin crust for much of
 547 the region, but not northern New York or southeastern Canada (Figure S15).



548

549 **Figure 6.** A summary of average crustal and mantle shear-wave velocity. (a) Average crustal
 550 shear-wave velocity map, (b) uppermost mantle shear-wave velocity map, and histograms of
 551 crustal V_s velocity (c) and uppermost mantle V_s velocity (d). The circles and rectangular boxes in
 552 (c) show locations of dated kimberlite intrusions and lithosphere anomalies from Chu et al.
 553 (2013), respectively. The mean (Avg.) of crustal V_s is 3.7 km/s with a standard derivation (Std.)
 554 of 0.1 km/s. The mean of uppermost mantle V_s is 4.51 km/s with a standard derivation of 0.03
 555 km/s. The dashed ellipses show the locations of two slow velocity anomalies described in the
 556 text. (For interpretation of the references to color in this figure, the reader is referred to the web
 557 version of this article.)

558 We do not see any evidence for slower mantle resulting from lithospheric delamination
 559 and upwelling that is evident in geochemical observations (Mazza et al., 2014). Thus if
 560 lithospheric delamination and mantle upwelling occurred as the rocks suggest, the feature must

561 be quite localized. The West Virginia-Virginia border overlies a relatively abrupt transition in
562 crustal thickness. The crust is relatively flat towards the Appalachian interior from west to east
563 but begins to thin near the area containing the kimberlite intrusions (see Figure 6b for the
564 locations). More evidence for a significant change in lithospheric structure across the region is
565 the difference in mid-crustal speed, which decreases by about 0.2-0.3 km/s from the
566 Appalachians eastward (see Figure 4b). Although the transition is smoother, the upper mantle
567 speed also decreases towards the east in the same region. The differences in structure suggest
568 interesting geologic differences throughout the lithosphere from the Appalachians to central and
569 eastern Virginia.

570 In Figure S16, we merged the EUS model with the published model in the western U.S.
571 (Chai et al., 2015). The smooth transition from west to east indicates that our EUS model is
572 compatible with the published western U.S. model. The anomalous upper mantle beneath the
573 western ME, the east coast, and New England is modest compared with that beneath the Basin
574 and Range province in the western U.S.

575 An automated cluster analysis (Chai et al., 2015) was used to group the 1-D shear
576 velocity profiles into clusters of similar Earth structure. The spatial distribution of the clusters
577 using shear velocities between the depth range of 5 and 200 km is shown in Figure S17. The
578 clustered velocity models are shown in Figure S18. The crust is thinner beneath western ME,
579 southern Basin and Range region, southern Interior Plains, and Atlantic Plain. A thicker crust
580 was imaged beneath western Interior Plains, Appalachian Highlands, Interior Highlands, central
581 Interior Plains. The southeastern Canadian Shield shows a slighter thinner crust. The upper
582 mantle is faster beneath the stable North America craton. The seismicity in the region does not
583 show a simple correlation to the subsurface seismic speed variation on the broad image in Figure
584 S18. The clusters obtained with shear velocities between the depth range of 0 to 20 km is shown
585 in Figure S19 and S20. To a certain extent, the distribution of clusters (Figure S19) can be used
586 as a guide to the choice of a local 1D velocity model for initial earthquake location or moment
587 tensor inversion. For instance, the same 1D velocity model may be used for the region specified
588 by the same cluster. We use more detailed cross-sections to explore the relationship between the
589 spatial distribution of earthquakes and subsurface structural variations.

590 **7 Discussion**

591 Large-scale regional lithospheric models contain many features that are often described
592 in a list of short commentary related to geology. Many of the structural features that we observed
593 have been pointed out in earlier studies (e.g., Chen Chen et al., 2016; Porter et al., 2016;
594 Schmandt et al., 2015; Shen & Ritzwoller, 2016); we noted several of these in the Results
595 section. One aspect not covered in other papers is the fact that a detailed crustal model provides
596 an opportunity to explore the relationship(s) between seismicity and subsurface structure (if any
597 exist). We use the cross-sections defined in Figure 1 to review the 3D model in details and to
598 explore potential relationships between structure and seismicity. The cross-sections were chosen
599 to cover most of the seismically active regions. Despite intensive studies, the cause of localized
600 seismicity in the region remains poorly understood. Many ideas have been proposed to explain
601 the intraplate seismicity of the EUS, such as stress concentration in regions of crustal weakness
602 or changes in lithospheric structure (Grana & Richardson, 1996; Grollmund & D. Zoback, 2001;
603 Kenner, 2000; Levandowski et al., 2016; Pollitz, 2001). Numerical models have shown that
604 crustal deformation can be induced at shallow depth when a dense anomaly resides in the crust

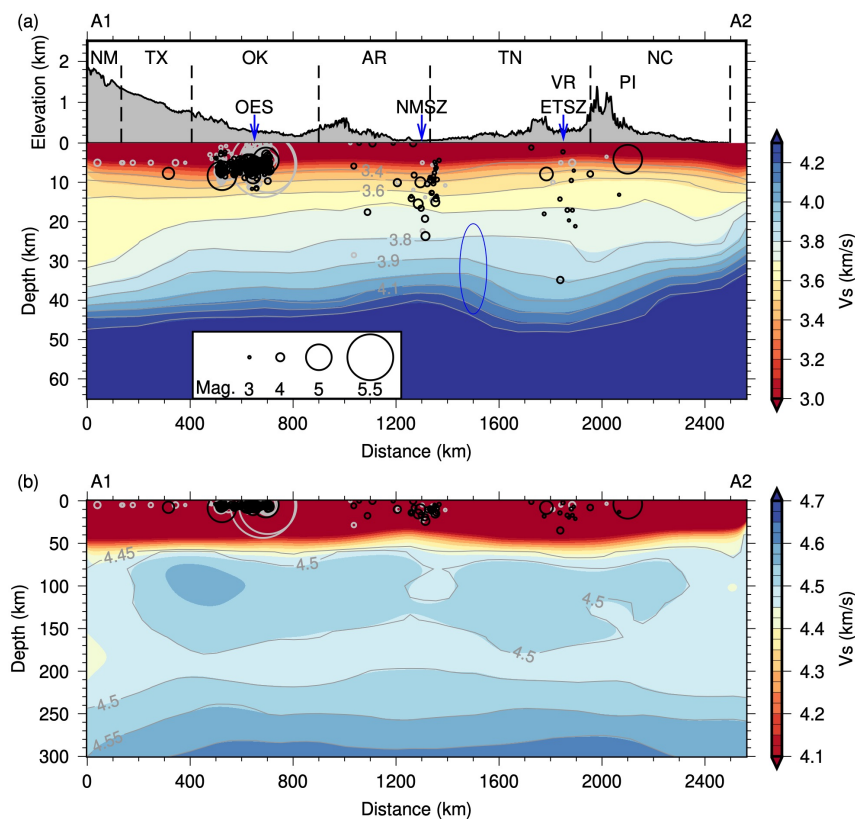
605 (Levandowski et al., 2016; Pollitz, 2001; Zhan et al., 2016) above a relatively weak upper
606 mantle. The depth and cause of a weak zone are still under debate (Chuanxu Chen et al., 2014;
607 Pollitz & Mooney, 2014). Since seismicity in Oklahoma may be related to human activity, we
608 skip that region (see Chai et al., 2021 for a detailed study of subsurface structure in that region).
609 But note that ultimately, the Oklahoma activity is a result of the geologic structure associated
610 with the hydrocarbon-rich basins in the area. The EUS model contains no significant features
611 deep beneath the Oklahoma seismic activity. Two regions of particular interest are the northern
612 ME and the Appalachian Mountains. We discussed some of the seismicity pattern and structure
613 relationships for New Madrid in the Results section.

614 The cross-section A1-A2 (Figure 7) passes through seismically active regions in
615 Oklahoma, the NMSZ, and the Eastern Tennessee Seismic Zone (ETSZ). The NMSZ is
616 underlain by a relatively fast lower crust, which has been interpreted as a mafic intrusion
617 (Catchings, 1999; Mooney et al., 1983). Reconstruction of the feature details is difficult with the
618 coarse 100-km sampling, but the broader scale model shows the slower mantle in comparison
619 with regions to the east and west. Numerical tests and Rayleigh-wave sensitivity kernels suggest
620 that our resolution begins to degrade at about 150 km (Figure S21), so we do not image the entire
621 feature. Nyamwandha et al. (2016) suggested that a Cretaceous thermal event producing these
622 anomalies is associated with upwelling fluids from the Farallon Slab, along with an already
623 weakened and thinned lithosphere as a result of interaction with the Bermuda Hot Spot roughly
624 80-100 Ma (Cox & Van Arsdale, 2002). The crustal thickness is a maximum beneath the Valley
625 and Ridge and decreases by about 10 km at the coastal region to the east. Although not
626 associated with seismicity, the cross-section indicates relatively higher mid-crust speeds beneath
627 the Piedmont region of North Carolina.

628 Seismicity in the ETSZ occurs on basement faults that have no surface expression
629 (Steltenpohl et al., 2010). Seismicity is located in the Valley and Ridge Province west of the
630 highest Appalachian elevations. A recent local earthquake tomography study imaged the
631 existence of the buried fault (Powell et al., 2014) as a low-velocity anomaly. The lateral extent of
632 the low anomaly is beyond the resolution of our velocity model. Our model contains a velocity
633 change in the lower crust beneath the ETSZ (ellipse in Figure 7), which may be associated with
634 the transition from the Granite-Rhyolite basement (west) to the Grenville basement (east) (Fisher
635 et al., 2010). Upper mantle shear velocity beneath the region is 2-3% faster than the mantle
636 beneath the NMSZ at depths of about 100 km.

637 The northwest-southeast striking cross-section B1-B2 (Figure 8) shows apparently
638 thinned crust beneath western North and South Dakota (solid ellipse) which is consistent with
639 Thurner et al. (2015) who argued that the apparently thin crust is actually a very fast underplated
640 crust in the vicinity of the 2 Ga Trans-Hudson Orogen. The model at what could be considered
641 uppermost mantle depths is relatively slow, so it is plausible to interpret the material as fast crust.
642 A region of apparently thin crust in southeastern North Dakota is more perplexing. Thurner et al.
643 (2015) estimated a crustal thickness of 30-35 km in this region. Our apparent crustal thickness is
644 slightly larger, about 38-40 km. To be fair, reverberations in the thin surface sedimentary cover
645 interfere with the Ps arrival from the apparent crust-mantle boundary, which may affect an
646 accurate estimation of the crust-mantle boundary. The multiples in receiver functions from the
647 apparent crust-mantle boundary are free of near-surface interference, which provide some
648 constraints on the boundary. The P-wave speeds in the apparent lower crust are in the 6.6-7.0
649 km/s range, not unusual, and the values increase to 7.8 sharply and reach values of 8.0-8.1 km/s

650 by a depth of 43 km. The region has relatively low heat flow (50-60 mW/m², Blackwell et al.,
 651 2011) though the data coverage is sparse. The apparently thinned crust may be a result of
 652 eclogite facies mafic material in the lowermost crust rendering the petrologic crust-mantle
 653 boundary seismically transparent (Furlong & Fountain, 1986; Griffin & O'Reilly, 1987). In
 654 cratonic areas, eclogite facies mafic material in the lowermost crust can have a P-wave speed
 655 larger than 8 km/s, which can lead to bias in the estimation of the crust-mantle boundary. Near
 656 the South Dakota Iowa border, the mid-crustal shear wave speed decreases relatively abruptly.
 657 The relatively slow mid-crust (see also in Visualization S1) from Iowa through Missouri may be
 658 related to a batholith inferred from the Missouri gravity low (Hildenbrand et al., 1996). The
 659 structure from Iowa through Missouri is relatively uniform until interrupted by the relatively fast
 660 lower crust beneath the NMSZ. The upper mantle beneath Iowa and Missouri is relatively fast
 661 and uniform across this region of relatively slow middle crust. To the southeast of the NMSZ, the
 662 middle crust again is relatively slow and the crust begins to thin (dashed ellipse in Figure 8) and
 663 the upper crust speed decreases near the Alabama-Georgia Border. The upper mantle below 100
 664 km, from the NMSZ to the southeast is one of the slowest profiles in the model, and includes the
 665 region believed to have been crossed by the Bermuda Hot Spot (Chu et al., 2013; Cox & Van
 666 Arsdale, 2002).

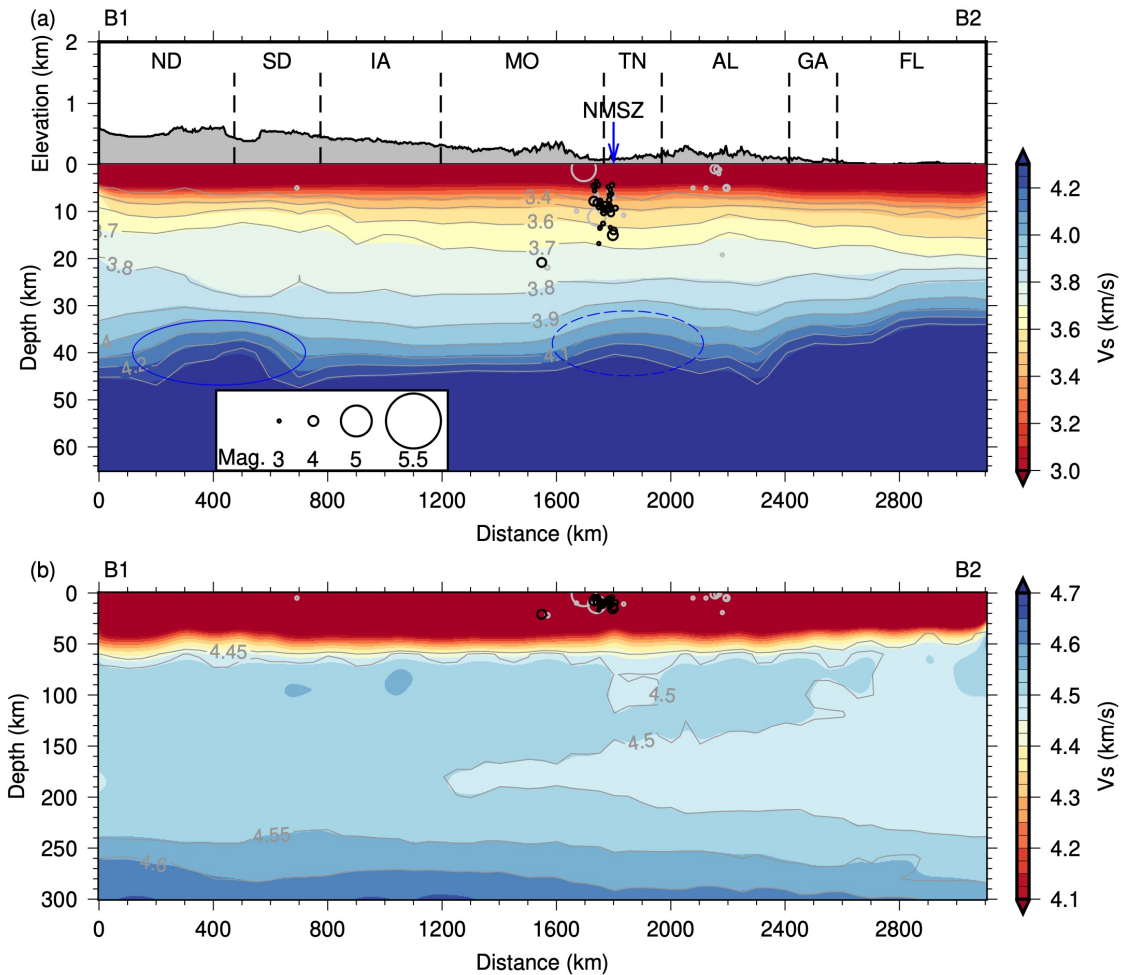


667

668 **Figure 7.** Shear velocity cross-sections along A1-A2. The panel (a) used a color palette for
 669 suitable crustal speeds. The panel (b) shows shear-wave speed changes in the upper mantle.
 670 Circles are earthquakes located within 100 km of the cross-section. Black circles are events with
 671 depth uncertainties less than 5 km. Gray circles represent earthquakes with larger depth
 672 uncertainties or without uncertainties. Note the image is vertically exaggerated.

673

674 Additional cross-sections can be found in Figure S22-S25 and discussed in Text S1. The
 675 inverted 3D seismic velocity model for the eastern United States is available in Data Set S1. The
 676 3D seismic velocity model for the western United States from Chai et al. (2015) is provided in
 677 Data Set S2. We also provide an interactive tool (Chai et al., 2018) to easily view the 3D model
 678 with depth slides and depth profiles side by side for both the eastern United States (Visualization
 679 S1) and the western United States (Visualization S2).



680

681 Figure 8. Same as Figure 7 but for cross-section B1-B2. The ellipses indicate anomalies
 682 described in the text.

683 7 Conclusions

684 Using spatially smoothed P-wave receiver functions, surface-wave dispersion, and
 685 Bouguer gravity observations, we construct 3D shear-wave velocity models in the EUS. The
 686 average crustal thickness of the EUS model is 43 km; the average crustal shear speed is 3.7 km/s;
 687 the average uppermost mantle shear-wave velocity in the model is 4.5 km/s. We imaged thinner
 688 crust beneath New England, the east coast, and the ME. The relative slow average shear-wave
 689 speeds in the mantle beneath New England and the southeastern US may be linked to hotspots.

690 Comparing to a compilation of basement age (Lund et al., 2015), regions with thin crust were
691 formed after 670 Ma, thicker crust in the cratonic region formed before 1000 Ma.

692 A comparison of seismicity and subsurface shear velocity suggests that often, but not
693 universally, earthquakes locate near regions with seismic velocity variation. However, not all
694 regions of significant subsurface seismic speed changes are loci of seismicity. The eastern
695 seaboard mantle appears slow, consistent with coarser, but deeper sampling models that have
696 been used as a basis for estimating dynamic topographic changes along the eastern seaboard
697 (Rowley et al., 2013). A weak correlation between upper mantle shear velocity and earthquake
698 focal mechanism has been observed. A relatively small upper mantle low-speed region in eastern
699 Kentucky and southwestern Ohio correlates with the area of perturbed upper mantle P-waves
700 analyzed by (Chu et al., 2013) which they associated with the circa 75 Ma kimberlite volcanic
701 site near Elliot Kentucky. The northern ME, and in particular the region of the large earthquakes
702 in 1811-12 appears to be underlain by a relatively fast lower crust and a relatively slow
703 uppermost mantle. Levandowski et al. (2016) suggested that such a structure can focus stress in
704 the upper crust, and our model is consistent with the idea.

705 **Acknowledgments, Samples, and Data**

706 Initial analyses for this work were performed at Pennsylvania State University. This work
707 was supported by the U.S. National Science Foundation (grants EAR-1053484 and EAR-
708 1053363) and by the U.S. Department of Energy (DOE), Office of Fossil Energy, Carbon
709 Storage Program through the Science-informed Machine Learning for Accelerating Real-Time
710 Decisions in Subsurface Applications (SMART) Initiative. The facilities of IRIS Data Services,
711 and specifically the IRIS Data Management Center, were used for access the waveforms, related
712 metadata, and/or derived products used in this study. See Table S1 for a full list of seismic
713 networks used in this study. IRIS Data Services are funded through the Seismological Facilities
714 for the Advancement of Geoscience and EarthScope (SAGE) Proposal of the National Science
715 Foundation under Cooperative Agreement EAR-1261681. Earthquake catalogs from U.S.
716 Geological Survey (<https://earthquake.usgs.gov/earthquakes/search/>, last accessed July, 2021)
717 and Saint Louis University Earthquake Center (Herrmann et al., 2011) were used in this study.
718 We acknowledge developers of Generic Mapping Tools version 5.4.4 (Paul Wessel et al., 2013)
719 and version 6.1.1 (P. Wessel et al., 2019), Obspy version 1.2.2 (Beyreuther et al., 2010; Krischer
720 et al., 2015; Megies et al., 2011), Numpy version 1.20.1 (Van Der Walt et al., 2011), Matplotlib
721 version 3.3.3 (Hunter, 2007), and Scikit-learn version 0.24.2 (Pedregosa et al., 2011) for sharing
722 their software packages. We thank University of California San Diego for sharing the STRM15
723 topography data that were used as background for several figures. We also thank National
724 Centers for Environmental Information for making ETOPO Global Relief Model available. The
725 boundaries of sedimentary basins were extracted from Coleman Jr. & Cahan (2012). This
726 manuscript has been authored in part by UT-Battelle, LLC, under contract DE- AC05-
727 00OR22725 with the US Department of Energy (DOE). The US government retains and the
728 publisher, by accepting the article for publication, acknowledges that the US government retains
729 a nonexclusive, paid-up, irrevocable, worldwide license to publish or reproduce the published
730 form of this manuscript, or allow others to do so, for US government purposes. DOE will
731 provide public access to these results of federally sponsored research in accordance with the
732 DOE Public Access Plan (<http://energy.gov/downloads/doe-public-access-plan>, last accessed in
733 May 2021). The views and conclusions contained in this document are those of the authors and
734 should not be interpreted as necessarily representing the official policies, either expressed or

735 implied, of the U.S. Government. The authors declare that they have no conflict of interest. The
 736 authors thank the Editor Maureen Long, Brian Savage, and an anonymous reviewer for their
 737 constructive comments.

738 **References**

- 739 Ammon, C. J. (1991). The isolation of receiver effects from teleseismic P -waveforms. *Bulletin*
 740 *of the Seismological Society of America*. <https://doi.org/10.1029/2005JB004161>
- 741 Ammon, C. J., Randall, G. E., & Zandt, G. (1990). On the nonuniqueness of receiver function
 742 inversions. *Journal of Geophysical Research*, *95*(B10), 15303.
 743 <https://doi.org/10.1029/JB095iB10p15303>
- 744 Balmino, G., Vales, N., Bonvalot, S., & Briais, A. (2012). Spherical harmonic modelling to ultra-
 745 high degree of Bouguer and isostatic anomalies. *Journal of Geodesy*, *86*(7), 499–520.
 746 <https://doi.org/10.1007/s00190-011-0533-4>
- 747 Bensen, G. D., Ritzwoller, M. H., Barmin, M. P., Levshin, A. L., Lin, F., Moschetti, M. P., et al.
 748 (2007). Processing seismic ambient noise data to obtain reliable broad-band surface wave
 749 dispersion measurements. *Geophysical Journal International*, *169*(3), 1239–1260.
 750 <https://doi.org/10.1111/j.1365-246X.2007.03374.x>
- 751 Beyreuther, M., Barsch, R., Krischer, L., Megies, T., Behr, Y., & Wassermann, J. (2010). ObsPy:
 752 A Python Toolbox for Seismology. *Seismological Research Letters*, *81*(3), 530–533.
 753 <https://doi.org/10.1785/gssrl.81.3.530>
- 754 Biryol, C. B., Wagner, L. S., Fischer, K. M., & Hawman, R. B. (2016). Relationship between
 755 observed upper mantle structures and recent tectonic activity across the Southeastern United
 756 States. *Journal of Geophysical Research: Solid Earth*, *121*(5), 3393–3414.
 757 <https://doi.org/10.1002/2015JB012698>
- 758 Biswas, N. N. (1972). Earth-flattening procedure for the propagation of Rayleigh wave. *Pure and*
 759 *Applied Geophysics PAGEOPH*, *96*(1), 61–74. <https://doi.org/10.1007/BF00875629>
- 760 Blackwell, D., Richards, M., Frone, Z., Batir, J., Ruzo, A., Dingwall, R., & Williams, M. (2011).
 761 Temperature at depth maps for the conterminous US and geothermal resource estimates.
 762 *Geothermal Resources Council Transactions* *35*, 1545–1550.
- 763 Bollmann, T. A., van der Lee, S., Frederiksen, A. W., Wolin, E., Revenaugh, J., Wiens, D. A., et
 764 al. (2019). P Wave Teleseismic Traveltime Tomography of the North American
 765 Midcontinent. *Journal of Geophysical Research: Solid Earth*, *124*(2), 1725–1742.
 766 <https://doi.org/10.1029/2018JB016627>
- 767 Catchings, R. D. (1999). Regional Vp, Vs, Vp/Vs, and Poisson's ratios across earthquake source
 768 zones from Memphis, Tennessee, to St. Louis, Missouri. *Bulletin of the Seismological*
 769 *Society of America*.
- 770 Chai, C., Ammon, C. J., Maceira, M., & Herrmann, R. B. (2015). Inverting interpolated receiver

- 771 functions with surface wave dispersion and gravity: Application to the western U.S. and
772 adjacent Canada and Mexico. *Geophysical Research Letters*, 42(11), 4359–4366.
773 <https://doi.org/10.1002/2015GL063733>
- 774 Chai, C., Ammon, C. J., Anandakrishnan, S., Ramirez, C., & Nyblade, A. (2017). Estimating
775 subglacial structure using P-wave receiver functions. *Geophysical Journal International*,
776 209(2), 1064–1079. <https://doi.org/10.1093/gji/ggx075>
- 777 Chai, C., Ammon, C. J., Maceira, M., & Herrmann, R. B. (2018). Interactive Visualization of
778 Complex Seismic Data and Models Using Bokeh. *Seismological Research Letters*, 89(2A),
779 668–676. <https://doi.org/10.1785/0220170132>
- 780 Chai, C., Delorey, A. A., Maceira, M., Levandowski, W., Guyer, R. A., Zhang, H., et al. (2021).
781 A 3D Full Stress Tensor Model for Oklahoma. *Journal of Geophysical Research: Solid*
782 *Earth*, 126(4), e2020JB021113. <https://doi.org/10.1029/2020JB021113>
- 783 Chen, Chen, Gilbert, H., Andronicos, C., Hamburger, M. W., Larson, T., Marshak, S., et al.
784 (2016). Shear velocity structure beneath the central United States: implications for the
785 origin of the Illinois Basin and intraplate seismicity. *Geochemistry, Geophysics,*
786 *Geosystems*, 17(3), 1020–1041. <https://doi.org/10.1002/2015GC006206>
- 787 Chen, Chuanxu, Zhao, D., & Wu, S. (2014). Crust and upper mantle structure of the New Madrid
788 Seismic Zone: Insight into intraplate earthquakes. *Physics of the Earth and Planetary*
789 *Interiors*, 230, 1–14. <https://doi.org/10.1016/j.pepi.2014.01.016>
- 790 Chong, J., Ni, S., Chu, R., & Somerville, P. (2016). Joint Inversion of Body-Wave Receiver
791 Function and Rayleigh-Wave Ellipticity. *Bulletin of the Seismological Society of America*,
792 106(2), 537–551. <https://doi.org/10.1785/0120150075>
- 793 Christensen, N. I., & Mooney, W. D. (1995). Seismic velocity structure and composition of the
794 continental crust: A global view. *Journal of Geophysical Research: Solid Earth*, 100(B6),
795 9761–9788. <https://doi.org/10.1029/95JB00259>
- 796 Chu, R., Leng, W., Helmberger, D. V., & Gurnis, M. (2013). Hidden hotspot track beneath the
797 eastern United States. *Nature Geoscience*, 6(11), 963–966.
798 <https://doi.org/10.1038/ngeo1949>
- 799 Coleman Jr., J. L., & Cahan, S. M. (2012). *Preliminary catalog of the sedimentary basins of the*
800 *United States*. Reston, VA. <https://doi.org/10.3133/ofr20121111>
- 801 Constable, S. C., Parker, R. L., & Constable, C. G. (1987). Occam's inversion: A practical
802 algorithm for generating smooth models from electromagnetic sounding data.
803 *GEOPHYSICS*, 52(3), 289–300. <https://doi.org/10.1190/1.1442303>
- 804 Cox, R. T., & Van Arsdale, R. B. (2002). The Mississippi Embayment, North America: a first
805 order continental structure generated by the Cretaceous superplume mantle event. *Journal*
806 *of Geodynamics*, 34(2), 163–176. [https://doi.org/10.1016/S0264-3707\(02\)00019-4](https://doi.org/10.1016/S0264-3707(02)00019-4)

- 807 Crotwell, H. P., & Owens, T. J. (2005). Automated Receiver Function Processing. *Seismological*
808 *Research Letters*, 76(6), 702–709. <https://doi.org/10.1785/gssrl.76.6.702>
- 809 Dong, M. T., & Menke, W. H. (2017). Seismic High Attenuation Region Observed Beneath
810 Southern New England From Teleseismic Body Wave Spectra: Evidence for High
811 Asthenospheric Temperature Without Melt. *Geophysical Research Letters*, 44(21), 10,958-
812 10,969. <https://doi.org/10.1002/2017GL074953>
- 813 Eaton, D. W., & Frederiksen, A. (2007). Seismic evidence for convection-driven motion of the
814 North American plate. *Nature*, 446(7134), 428–431. <https://doi.org/10.1038/nature05675>
- 815 Ekström, G. (2011). A global model of Love and Rayleigh surface wave dispersion and
816 anisotropy, 25-250 s. *Geophysical Journal International*, 187(3), 1668–1686.
817 <https://doi.org/10.1111/j.1365-246X.2011.05225.x>
- 818 Ekström, G. (2014). Love and Rayleigh phase-velocity maps, 5–40 s, of the western and central
819 USA from USArray data. *Earth and Planetary Science Letters*, 402, 42–49.
820 <https://doi.org/10.1016/j.epsl.2013.11.022>
- 821 Faill, R. T. (1998). A geologic history of the north-central Appalachians; Part 3, The Alleghany
822 Orogeny. *American Journal of Science*, 298(2), 131–179.
823 <https://doi.org/10.2475/ajs.298.2.131>
- 824 Fisher, C. M., Loewy, S. L., Miller, C. F., Berquist, P., Van Schmus, W. R., Hatcher, R. D., et al.
825 (2010). Whole-rock Pb and Sm-Nd isotopic constraints on the growth of southeastern
826 Laurentia during Grenvillian orogenesis. *Geological Society of America Bulletin*, 122(9–
827 10), 1646–1659. <https://doi.org/10.1130/B30116.1>
- 828 Furlong, K. P., & Fountain, D. M. (1986). Continental crustal underplating: Thermal
829 considerations and seismic-petrologic consequences. *Journal of Geophysical Research*,
830 91(B8), 8285. <https://doi.org/10.1029/JB091iB08p08285>
- 831 Golos, E. M., Fang, H., Yao, H., Zhang, H., Burdick, S., Vernon, F., et al. (2018). Shear Wave
832 Tomography Beneath the United States Using a Joint Inversion of Surface and Body
833 Waves. *Journal of Geophysical Research: Solid Earth*, 123(6), 5169–5189.
834 <https://doi.org/10.1029/2017JB014894>
- 835 Grana, J. P., & Richardson, R. M. (1996). Tectonic stress within the New Madrid seismic zone.
836 *Journal of Geophysical Research: Solid Earth*, 101(B3), 5445–5458.
837 <https://doi.org/10.1029/95JB03255>
- 838 Griffin, W. L., & O'Reilly, S. Y. (1987). Is the continental Moho the crust-mantle boundary?
839 *Geology*, 15(3), 241. [https://doi.org/10.1130/0091-7613\(1987\)15<241:ITCMTC>2.0.CO;2](https://doi.org/10.1130/0091-7613(1987)15<241:ITCMTC>2.0.CO;2)
- 840 Grollmund, B., & D. Zoback, M. (2001). Did deglaciation trigger intraplate seismicity in the
841 New Madrid seismic zone? *Geology*, 29(2), 175. [https://doi.org/10.1130/0091-7613\(2001\)029<0175:DDTISI>2.0.CO;2](https://doi.org/10.1130/0091-7613(2001)029<0175:DDTISI>2.0.CO;2)
842

- 843 Hames, W. E., Renne, P. R., & Ruppel, C. (2000). New evidence for geologically instantaneous
844 emplacement of earliest Jurassic Central Atlantic magmatic province basalts on the North
845 American margin. *Geology*, 28(9), 859. [https://doi.org/10.1130/0091-](https://doi.org/10.1130/0091-7613(2000)28<859:NEFGIE>2.0.CO;2)
846 [7613\(2000\)28<859:NEFGIE>2.0.CO;2](https://doi.org/10.1130/0091-7613(2000)28<859:NEFGIE>2.0.CO;2)
- 847 Hatcher, R. D. (2010). The Appalachian orogen: A brief summary (pp. 1–19).
848 [https://doi.org/10.1130/2010.1206\(01\)](https://doi.org/10.1130/2010.1206(01))
- 849 Herrmann, R. B., Benz, H., & Ammon, C. J. (2011). Monitoring the Earthquake Source Process
850 in North America. *Bulletin of the Seismological Society of America*, 101(6), 2609–2625.
851 <https://doi.org/10.1785/0120110095>
- 852 Herrmann, R. B., Ammon, C. J., Benz, H. M., Aziz-Zanjani, A., & Boschelli, J. (2021). Short-
853 Period Surface-Wave Tomography in the Continental United States—A Resource for
854 Research. *Seismological Research Letters*, 92(6), 3642–3656.
855 <https://doi.org/10.1785/0220200462>
- 856 Hildenbrand, T. G., Griscom, A., Van Schmus, W. R., & Stuart, W. D. (1996). Quantitative
857 investigations of the Missouri gravity low: A possible expression of a large, Late
858 Precambrian batholith intersecting the New Madrid seismic zone. *Journal of Geophysical*
859 *Research: Solid Earth*, 101(B10), 21921–21942. <https://doi.org/10.1029/96JB01908>
- 860 Hough, S. E., Armbruster, J. G., Seeber, L., & Hough, J. F. (2000). On the Modified Mercalli
861 intensities and magnitudes of the 1811-1812 New Madrid earthquakes. *Journal of*
862 *Geophysical Research: Solid Earth*, 105(B10), 23839–23864.
863 <https://doi.org/10.1029/2000JB900110>
- 864 Hunter, J. D. (2007). Matplotlib: a 2D graphics environment. *Computing in Science &*
865 *Engineering*, 9(3), 90–95. <https://doi.org/10.1109/MCSE.2007.55>
- 866 Hynes, A., & Rivers, T. (2010). Protracted continental collision - evidence from the Grenville
867 Orogen. *Canadian Journal of Earth Sciences*, 47(5), 591–620. [https://doi.org/10.1139/E10-](https://doi.org/10.1139/E10-003)
868 [003](https://doi.org/10.1139/E10-003)
- 869 Jin, G., & Gaherty, J. B. (2015). Surface wave phase-velocity tomography based on multichannel
870 cross-correlation. *Geophysical Journal International*, 201(3), 1383–1398.
871 <https://doi.org/10.1093/gji/ggv079>
- 872 Johnston, A. C. (1996). Seismic moment assessment of earthquakes in stable continental regions-
873 III. New Madrid 1811-1812, Charleston 1886 and Lisbon 1755. *Geophysical Journal*
874 *International*, 126(2), 314–344. <https://doi.org/10.1111/j.1365-246X.1996.tb05294.x>
- 875 Julià, J., Ammon, C. J., Herrmann, R. B., & Correig, A. M. (2000). Joint inversion of receiver
876 function and surface wave dispersion observations. *Geophysical Journal International*,
877 *143*(1), 99–112. <https://doi.org/10.1046/j.1365-246x.2000.00217.x>
- 878 Julià, J., Ammon, C. J., & Herrmann, R. B. (2003). Lithospheric structure of the Arabian Shield
879 from the joint inversion of receiver functions and surface-wave group velocities.

- 880 *Tectonophysics*, 371(1–4), 1–21. [https://doi.org/10.1016/S0040-1951\(03\)00196-3](https://doi.org/10.1016/S0040-1951(03)00196-3)
- 881 Kenner, S. J. (2000). A Mechanical Model for Intraplate Earthquakes: Application to the New
882 Madrid Seismic Zone. *Science*, 289(5488), 2329–2332.
883 <https://doi.org/10.1126/science.289.5488.2329>
- 884 Kennett, B. L. N., Engdahl, E. R., & Buland, R. (1995). Constraints on seismic velocities in the
885 Earth from traveltimes. *Geophysical Journal International*, 122(1), 108–124.
886 <https://doi.org/10.1111/j.1365-246X.1995.tb03540.x>
- 887 Krischer, L., Megies, T., Barsch, R., Beyreuther, M., Lecocq, T., Caudron, C., & Wassermann, J.
888 (2015). ObsPy: a bridge for seismology into the scientific Python ecosystem.
889 *Computational Science & Discovery*, 8(1), 014003. [https://doi.org/10.1088/1749-](https://doi.org/10.1088/1749-4699/8/1/014003)
890 [4699/8/1/014003](https://doi.org/10.1088/1749-4699/8/1/014003)
- 891 Langston, C. A. (1979). Structure under Mount Rainier, Washington, inferred from teleseismic
892 body waves. *Journal of Geophysical Research*, 84(B9), 4749.
893 <https://doi.org/10.1029/JB084iB09p04749>
- 894 Langston, C. A. (2011). Wave-Field Continuation and Decomposition for Passive Seismic
895 Imaging Under Deep Unconsolidated Sediments. *Bulletin of the Seismological Society of*
896 *America*, 101(5), 2176–2190. <https://doi.org/10.1785/0120100299>
- 897 Laske, G., Masters, G., Ma, Z., & Pasyanos, M. (2013). Update on CRUST1. 0-A 1-degree
898 global model of Earth's crust. *EGU General Assembly*, 15, 2658.
- 899 Levandowski, W., Boyd, O. S., & Ramirez-Guzmán, L. (2016). Dense lower crust elevates long-
900 term earthquake rates in the New Madrid seismic zone. *Geophysical Research Letters*,
901 43(16), 8499–8510. <https://doi.org/10.1002/2016GL070175>
- 902 Li, Q., Liu, M., Zhang, Q., & Sandvol, E. (2007). Stress evolution and seismicity in the central-
903 eastern United States: Insights from geodynamic modeling. In *Special Paper 425:*
904 *Continental Intraplate Earthquakes: Science, Hazard, and Policy Issues* (pp. 149–166).
905 Geological Society of America. [https://doi.org/10.1130/2007.2425\(11\)](https://doi.org/10.1130/2007.2425(11))
- 906 Ligorria, J. P., & Ammon, C. J. (1999). Iterative deconvolution and receiver-function estimation.
907 *Bulletin of the Seismological Society of America*, 89(5), 1395–1400.
- 908 Lund, K., Box, S. E., Holm-Denoma, C., San Juan, C. A., Blakely, R. J., Saltus, R. W., et al.
909 (2015). *Basement Domain Map of the Conterminous United States and Alaska*. U.S.
910 *Geological Survey Data Series 898*. <https://doi.org/10.3133/ds898>
- 911 Maceira, M., & Ammon, C. J. (2009). Joint inversion of surface wave velocity and gravity
912 observations and its application to central Asian basins shear velocity structure. *Journal of*
913 *Geophysical Research*, 114(B2), B02314. <https://doi.org/10.1029/2007JB005157>
- 914 Mazza, S. E., Gazel, E., Johnson, E. A., Kunk, M. J., McAleer, R., Spotila, J. A., et al. (2014).
915 Volcanoes of the passive margin: The youngest magmatic event in eastern North America.

- 916 *Geology*, 42(6), 483–486. <https://doi.org/10.1130/G35407.1>
- 917 Megies, T., Beyreuther, M., Barsch, R., Krischer, L., & Wassermann, J. (2011). ObsPy - what
918 can it do for data centers and observatories? *Annals of Geophysics*, 54(1), 47–58.
919 <https://doi.org/10.4401/ag-4838>
- 920 Menke, W., Lamoureux, J., Abbott, D., Hopper, E., Hutson, D., & Marrero, A. (2018). Crustal
921 Heating and Lithospheric Alteration and Erosion Associated With Asthenospheric
922 Upwelling Beneath Southern New England (USA). *Journal of Geophysical Research: Solid*
923 *Earth*, 123(10), 8995–9008. <https://doi.org/10.1029/2018JB015921>
- 924 Mooney, W. D., Andrews, M. C., Ginzburg, A., Peters, D. A., & Hamilton, R. M. (1983). Crustal
925 Structure of the Northern Mississippi Embayment and a Comparison with other Continental
926 Rift Zones. In *Developments in Geotectonics* (pp. 327–348). <https://doi.org/10.1016/B978-0-444-42198-2.50025-0>
- 927
- 928 Newman, A. (1999). Slow Deformation and Lower Seismic Hazard at the New Madrid Seismic
929 Zone. *Science*, 284(5414), 619–621. <https://doi.org/10.1126/science.284.5414.619>
- 930 Nyamwandha, C. A., Powell, C. A., & Langston, C. A. (2016). A joint local and teleseismic
931 tomography study of the Mississippi Embayment and New Madrid Seismic Zone. *Journal*
932 *of Geophysical Research: Solid Earth*, 121(5), 3570–3585.
933 <https://doi.org/10.1002/2015JB012761>
- 934 Özalaybey, S., Savage, M. K., Sheehan, A. F., Louie, J. N., & Brune, J. N. (1997). Shear-wave
935 velocity structure in the northern Basin and Range province from the combined analysis of
936 receiver functions and surface waves. *Bulletin of the Seismological Society of America*,
937 87(1), 183–199.
- 938 Paige, C. C., & Saunders, M. A. (1982). LSQR: An Algorithm for Sparse Linear Equations and
939 Sparse Least Squares. *ACM Transactions on Mathematical Software*, 8(1), 43–71.
940 <https://doi.org/10.1145/355984.355989>
- 941 Pavlis, N. K., Holmes, S. A., Kenyon, S. C., & Factor, J. K. (2012). The development and
942 evaluation of the Earth Gravitational Model 2008 (EGM2008). *Journal of Geophysical*
943 *Research: Solid Earth*, 117(B4), B04406. <https://doi.org/10.1029/2011JB008916>
- 944 Pedregosa, F., Varoquaux, G., Gramfort, A., Michel, V., Thirion, B., Grisel, O., et al. (2011).
945 Scikit-learn: Machine Learning in Python. *Journal of Machine Learning Research*, 12,
946 2825–2830.
- 947 Plouff, D. (1976). Gravity and magnetic fields of polygonal prisms and application to magnetic
948 terrain corrections. *Geophysics*, 41(4), 727–741. <https://doi.org/10.1190/1.1440645>
- 949 Pollitz, F. F. (2001). Sinking Mafic Body in a Reactivated Lower Crust: A Mechanism for Stress
950 Concentration at the New Madrid Seismic Zone. *Bulletin of the Seismological Society of*
951 *America*, 91(6), 1882–1897. <https://doi.org/10.1785/0120000277>

- 952 Pollitz, F. F., & Mooney, W. D. (2014). Seismic structure of the Central US crust and shallow
953 upper mantle: Uniqueness of the Reelfoot Rift. *Earth and Planetary Science Letters*, 402,
954 157–166. <https://doi.org/10.1016/j.epsl.2013.05.042>
- 955 Porter, R., Liu, Y., & Holt, W. E. (2016). Lithospheric records of orogeny within the continental
956 U.S. *Geophysical Research Letters*, 43(1), 144–153. <https://doi.org/10.1002/2015GL066950>
- 957 Powell, C. A., Withers, M. M., Cox, R. T., Vlahovic, G., & Arroucau, P. (2014). Crustal velocity
958 structure associated with the eastern Tennessee seismic zone: Vp and Vs images based upon
959 local earthquake tomography. *Journal of Geophysical Research: Solid Earth*, 119(1), 464–
960 489. <https://doi.org/10.1002/2013JB010433>
- 961 Rowley, D. B., Forte, A. M., Moucha, R., Mitrovica, J. X., Simmons, N. A., & Grand, S. P.
962 (2013). Dynamic topography change of the Eastern United States since 3 million years ago.
963 *Science*, 340(6140), 1560–1563. <https://doi.org/10.1126/science.1229180>
- 964 Saito, M. (1988). Disper80: A subroutine package for the calculation of seismic normal-mode
965 solutions. In *Seismological algorithms* (pp. 293–319). Academic Press.
- 966 Savage, B., Covellone, B. M., & Shen, Y. (2017). Wave speed structure of the eastern North
967 American margin. *Earth and Planetary Science Letters*, 459, 394–405.
968 <https://doi.org/10.1016/j.epsl.2016.11.028>
- 969 Savage, Brian. (2021). Body Wave Speed Structure of Eastern North America. *Geochemistry,*
970 *Geophysics, Geosystems*, 22(1), 1–18. <https://doi.org/10.1029/2020GC009002>
- 971 Schmandt, B., Lin, F.-C., & Karlstrom, K. E. (2015). Distinct crustal isostasy trends east and
972 west of the Rocky Mountain Front. *Geophysical Research Letters*, 42(23), 10,290–10,298.
973 <https://doi.org/10.1002/2015GL066593>
- 974 Shen, W., & Ritzwoller, M. H. (2016). Crustal and uppermost mantle structure beneath the
975 United States. *Journal of Geophysical Research: Solid Earth*, 121(6), 4306–4342.
976 <https://doi.org/10.1002/2016JB012887>
- 977 Stein, S. (2007). Approaches to continental intraplate earthquake issues. In *Special Paper 425:*
978 *Continental Intraplate Earthquakes: Science, Hazard, and Policy Issues* (pp. 1–16).
979 Geological Society of America. [https://doi.org/10.1130/2007.2425\(01\)](https://doi.org/10.1130/2007.2425(01))
- 980 Steltenpohl, M. G., Zietz, I., Horton, J. W., & Daniels, D. L. (2010). New York–Alabama
981 lineament: A buried right-slip fault bordering the Appalachians and mid-continent North
982 America. *Geology*, 38(6), 571–574. <https://doi.org/10.1130/G30978.1>
- 983 Sun, X., Bao, X., Xu, M., Eaton, D. W., Song, X., Wang, L., et al. (2014). Crustal structure
984 beneath SE Tibet from joint analysis of receiver functions and Rayleigh wave dispersion.
985 *Geophysical Research Letters*, 41(5), 1479–1484. <https://doi.org/10.1002/2014GL059269>
- 986 Thurner, S., Margolis, R., Levander, A., & Niu, F. (2015). PdS receiver function evidence for
987 crustal scale thrusting, relic subduction, and mafic underplating in the Trans-Hudson

- 988 Orogen and Yavapai province. *Earth and Planetary Science Letters*, 426, 13–22.
989 <https://doi.org/10.1016/j.epsl.2015.06.007>
- 990 Tuttle, M. P. (2002). The Earthquake Potential of the New Madrid Seismic Zone. *Bulletin of the*
991 *Seismological Society of America*, 92(6), 2080–2089. <https://doi.org/10.1785/0120010227>
- 992 Wagner, L. S., Fischer, K. M., Hawman, R., Hopper, E., & Howell, D. (2018). The relative roles
993 of inheritance and long-term passive margin lithospheric evolution on the modern structure
994 and tectonic activity in the southeastern United States. *Geosphere*, 14(4), 1385–1410.
995 <https://doi.org/10.1130/GES01593.1>
- 996 Van Der Walt, S., Colbert, S. C., & Varoquaux, G. (2011). The NumPy array: A structure for
997 efficient numerical computation. *Computing in Science and Engineering*, 13(2), 22–30.
998 <https://doi.org/10.1109/MCSE.2011.37>
- 999 Wessel, P., Luis, J. F., Uieda, L., Scharroo, R., Wobbe, F., Smith, W. H. F., & Tian, D. (2019).
1000 The Generic Mapping Tools Version 6. *Geochemistry, Geophysics, Geosystems*, 20(11),
1001 5556–5564. <https://doi.org/10.1029/2019GC008515>
- 1002 Wessel, Paul, Smith, W. H. F., Scharroo, R., Luis, J., & Wobbe, F. (2013). Generic Mapping
1003 Tools: improved version released. *Eos, Transactions American Geophysical Union*, 94(45),
1004 409–410. <https://doi.org/10.1002/2013EO450001>
- 1005 Whitmeyer, S. (2007). Tectonic model for the Proterozoic growth of North America. *Geosphere*,
1006 3(4), 220. <https://doi.org/10.1130/GES00055.1>
- 1007 Yang, B. B., Gao, S. S., Liu, K. H., Elsheikh, A. A., Lemnifi, A. A., Refayee, H. A., & Yu, Y.
1008 (2014). Seismic anisotropy and mantle flow beneath the northern Great Plains of North
1009 America. *Journal of Geophysical Research: Solid Earth*, 119(3), 1971–1985.
1010 <https://doi.org/10.1002/2013JB010561>
- 1011 Yang, X., Pavlis, G. L., & Wang, Y. (2016). A Quality Control Method for Teleseismic P -Wave
1012 Receiver Functions. *Bulletin of the Seismological Society of America*, 106(5), 1948–1962.
1013 <https://doi.org/10.1785/0120150347>
- 1014 Zhan, Y., Hou, G., Kusky, T., & Gregg, P. M. (2016). Stress development in heterogenetic
1015 lithosphere: Insights into earthquake processes in the New Madrid Seismic Zone.
1016 *Tectonophysics*, 671, 56–62. <https://doi.org/10.1016/j.tecto.2016.01.016>
- 1017 Zhu, L. (2000). Crustal structure across the San Andreas Fault, southern California from
1018 teleseismic converted waves. *Earth and Planetary Science Letters*, 179(1), 183–190.
1019 [https://doi.org/10.1016/S0012-821X\(00\)00101-1](https://doi.org/10.1016/S0012-821X(00)00101-1)
- 1020 Zhu, L., & Kanamori, H. (2000). Moho depth variation in southern California from teleseismic
1021 receiver functions. *Journal of Geophysical Research: Solid Earth*, 105(B2), 2969–2980.
1022 <https://doi.org/10.1029/1999JB900322>